

1 **The Origin of Continental Carbonates in Andean Salars:**  
2 **A Multi-Tracer Geochemical Approach in Laguna Pastos Grandes (Bolivia)**

3 E. Muller<sup>1</sup>, E. C. Gaucher<sup>2</sup>, C. Durllet<sup>3</sup>, J.S. Moquet<sup>1</sup>, M. Moreira<sup>1</sup>, V. Rouchon<sup>4</sup>, P.  
4 Louvat<sup>1</sup>, G. Bardoux<sup>1</sup>, S. Noirez<sup>4</sup>, C. Bougeault<sup>3</sup>, E. Vennin<sup>3</sup>, E. Gérard<sup>1</sup>, M. Chavez<sup>5</sup>, A.  
5 Virgone<sup>2</sup>, M. Ader<sup>1</sup>

6 <sup>1</sup>Université de Paris, Institut de physique du globe de Paris, CNRS, F-75005 Paris, France

7 <sup>2</sup>Total CSTJF, Avenue Larribau, 64018 Pau Cedex, France

8 <sup>3</sup>Biogéosciences, UMR 6282 CNRS, 6 boulevard Gabriel, Université Bourgogne  
9 Franche-Comté, 21000 Dijon, France

10 <sup>4</sup>IFP Energies Nouvelles, 1-4 Avenue de Bois Préau, 92852, Rueil-Malmaison Cedex,  
11 France

12 <sup>5</sup>Total E&P, 40 Calle Las Violetas, Edificio Arcus, Santa Cruz de la Sierra, Bolivia

13 Corresponding author: Elodie Muller (emuller@ipgp.fr)

14 **This article is a non-peer reviewed preprint submitted to EarthArXiv and under**  
15 **review in *Geochimica and Cosmochimica Acta*.**

16 **Abstract**

17 In continental volcanic settings, abundant carbonate precipitation can occur with  
18 atypical facies compared with those of marine settings. The (bio-)chemical processes  
19 responsible for their development and early diagenesis are typically complex and not fully  
20 understood. In the Bolivian Altiplano, Laguna Pastos Grandes hosts a 40-km<sup>2</sup> carbonate  
21 platform composed of a great diversity of carbonate facies mainly fed by thermal springs.  
22 It provides for a spectacular natural laboratory for studying carbonate precipitation in a  
23 continental province dominated by volcanism. As a first step toward understanding the  
24 processes responsible for the precipitation of carbonates in Laguna Pastos Grandes, we will  
25 focus on characterizing the fluids (liquid and gas) that feed the laguna. The content of major  
26 elements and stable isotope compositions ( $\delta^2\text{H}$ - $\delta^{18}\text{O}$ ,  $\delta^{37}\text{Cl}$ ,  $\delta^7\text{Li}$ ,  $\delta^{11}\text{B}$  and  $^{87}\text{Sr}/^{86}\text{Sr}$ ) of  
27 brine and freshwater inputs were investigated to trace the origin of both water and solutes  
28 in the laguna. The stable isotope compositions ( $\delta^{13}\text{C}$ ,  $\delta^{15}\text{N}$ ) and noble gas isotope ratios of  
29 outgassing at the laguna's floor were also determined. The results show that thermal  
30 springs are close to saturation with calcite. PHREEQC modeling of the hydrological  
31 system, together with gas geochemistry results and temperature estimated from a  
32 combination of geothermometers, indicates that Ca in these springs is inherited from the  
33 alteration of the volcanic bedrock by aqueous fluids heated at  $\sim 225$  °C and highly enriched  
34 in magmatic mantle-derived CO<sub>2</sub>. Our results clearly show that the main driver for the  
35 precipitation of modern carbonates in the Central Andes is the deeply sourced CO<sub>2</sub>, which  
36 boosts the alteration of volcanic rocks at depth.

37 **1. Introduction**

38 Continental volcanic provinces are not known for their abundance in terrestrially formed  
39 carbonate deposits. Volcanoclastic, bio-silica, clay or evaporitic sediments are typically  
40 dominant. However, it has long been documented that carbonates can also form, in varying

41 abundances, both in pedogenetic profiles (see synthesis in Zamanian et al., 2017; Durand  
42 et al., 2018) and in palustro-lacustro contexts (see synthesis in Alonso-Zarza and Tanner,  
43 2010; Verrecchia, 2017). Such continental carbonates have been generally less studied than  
44 marine ones, which have been considered as common hydrocarbon reservoirs and  
45 traditional archives for past oceans since the Archean. Yet, the recent discovery of  
46 hydrocarbon plays in Lower Cretaceous continental carbonates off the Brazilian coast  
47 helped change that view (Terra et al., 2010; Tosca and Wright, 2015) and promoted various  
48 and numerous studies into the origin and occurrence of carbonates in continental areas  
49 where the catchment and underlying rocks are mainly volcanic (Teboul et al., 2016; 2017).

50 Laguna Pastos Grandes in southern Bolivia exhibits a ~40 km<sup>2</sup> recent to modern carbonate  
51 platform making it unique among the more than 200 salars scattered across the volcanic  
52 Central Andes region (Fig. 1a, b). Laguna Negra in Argentina is the only other Andean  
53 salar recently described with a significant, but much smaller (6.5 km<sup>2</sup>; Gomez et al., 2014),  
54 carbonate platform. Laguna Pastos Grandes exhibits a great diversity of calcitic, siliceous  
55 and evaporitic fabrics deposited in palustrine to shallow lacustrine environments, including  
56 some of the largest modern pisoliths discovered to date (Fig. 1c; Risacher and Eugster,  
57 1979; Jones and Renaut, 1994; Bougeault et al., 2019). In some ways, it may be considered  
58 as a modern equivalent of carbonate facies and processes that occurred during  
59 sedimentation of the Presalt facies in the volcanic-rich South Atlantic realm during the  
60 Early Cretaceous.

61 Despite several studies already conducted on the hydrology and origin of chemical  
62 sediments in Bolivian and Chilean salars, no clear evidence appears to explain the  
63 abundance of modern carbonates in Laguna Pastos Grandes. From structural, hydrological  
64 and lithological points of view, this seems to occur in similar environments than salars  
65 where carbonates are absent or not modern (Risacher et al., 2003; Risacher and Fritz, 2009;  
66 see geological setting). Although climatic parameters fundamentally control the existence  
67 and morphology of salars (Risacher and Fritz, 2009), the chemical composition of the  
68 brines and the nature of the precipitates in these lakes depend on the initial composition of  
69 the inflow waters. In the present study, we thus performed a comprehensive geochemical  
70 study of gases and waters discharging in the carbonate platform of Laguna Pastos Grandes  
71 and brine filling the main basin.

72 The overarching goal of our research is to better understand the ongoing processes that  
73 allow for the rapid growth of these continental carbonates in a volcanic area under  
74 structural extension and fed by hydrothermal fluids. As a first step, this study focuses on  
75 the origin of the fluids and solutes from which carbonates have formed in the laguna based  
76 on the study of: (i) the chemical compositions of both water samples from streams of the  
77 drainage area and hydrothermal springs upwelling through or near the carbonate platform  
78 and gas associated with the hydrothermal springs; (ii) the isotopic compositions of gas  
79 components ( $\delta^{13}\text{C}$ ,  $\delta^{15}\text{N}$  and noble gases), water samples ( $\delta^2\text{H}$  and  $\delta^{18}\text{O}$ ) and some of their  
80 solutes ( $\delta^{37}\text{Cl}$ ,  $\delta^7\text{Li}$ ,  $\delta^{11}\text{B}$  and  $^{87}\text{Sr}/^{86}\text{Sr}$ ); and (iii) Li, B and Sr isotopic compositions of  
81 volcanic rock samples surrounding the salar. These results, together with the temperature  
82 of the underlying geothermal reservoir estimated from a combination of geothermometers  
83 and PHREEQC modeling of the hydrological system allowed us to discuss the main factors

84 responsible for the high precipitation of modern carbonates in Laguna Pastos Grandes  
85 compared with the other Andean salars.

## 86 **2. Geological Setting**

87 Laguna Pastos Grandes is located in the southern part of the Bolivian Altiplano, in the  
88 South Lipez region. The Altiplano (3700 – 4500 m) is a major Plio-Pleistocene continental  
89 plateau bounded by the Eastern and Western Cordilleras and dominated by Cenozoic  
90 stratovolcanoes and their products (Fig. 1). To the south, rhyolitic ignimbrites and dacites  
91 to rhyodacites of the Altiplano-Puna Volcanic Complex (APVC) dominate the South Lipez  
92 region, whereas andesites to dacites predominate on the Chilean side (Thorpe et al., 1976).  
93 Native sulfur deposits occur on many of the volcanoes in Chile, and thermal springs are  
94 abundant. A thick succession of Cretaceous and Tertiary continental sediments, including  
95 evaporite deposits, has been observed in the Bolivian Eastern Cordillera and could be  
96 covered by volcanic rocks toward the west in the studied area (Kusmaul et al., 1977;  
97 Deconinck et al., 2000).

98  
99 There are more than 200 closed basin lakes in the Bolivian Altiplano and Chilean Western  
100 Cordillera (Ericksen and Salas, 1987; Luddington et al., 1992). Most are saline and  
101 encompass a wide range of perennial or ephemeral lakes, locally termed “salar”. The two  
102 largest salars, Uyuni and Coipasa, are remnants of larger Pleistocene lakes and occupy the  
103 lower part of the Altiplano (3650 m altitude), whereas an abundance of smaller evaporitic  
104 basins (<400 km<sup>2</sup>) occur at higher elevations (4000–4500 m) of the southern Altiplano  
105 (Fig. 1). The presence of these southern basins and their morphology are firstly due to the  
106 cold and dry climate of this region with a mean annual precipitation of 100-200 mm (Iltis  
107 et al., 1984) that mostly falls in summer (December-March); air temperatures ranging from  
108 -30 °C in winter (May-August) to 25 °C in summer with daytime fluctuations of up to 40  
109 °C (Risacher and Fritz, 1991); high insolation; and annual evaporation of approximately  
110 1400 mm (Servant-Vildary and Roux, 1990). Although they belong to relatively similar  
111 environments in terms of geology and climate, they show a large variety of brine  
112 compositions, which can be organized into three major groups: alkaline, sulfate-rich, and  
113 calcium-rich brines (Risacher and Fritz, 2009). Different precipitates can be found in  
114 association with these brines, the most common being sodium chloride; sodium sulfates to  
115 borates; sodium carbonates; and calcium sulfates (Ahlfeld, 1956; Ahlfeld and Branisa,  
116 1960). Their formation and evolution have been suggested to result from the combination  
117 of two basic factors: the presence of interior drainage basins as a source of solutes and high  
118 rates of evaporation implying salt deposition (Risacher et al., 2003). Inflows to the Andean  
119 salars stem from a variety of sources such as permanent and ephemeral streams; shoreline  
120 springs; groundwater discharge; and thermal springs. Most of the rainwater falling on the  
121 drainage area infiltrates and recharges underlying aquifers. Shoreline spring and hot-spring  
122 waters are typically enriched in solutes compared with streams due to the dissolution of  
123 ancient and/or present-day evaporitic sediments or by the infiltration and recycling of lake  
124 brines. Therefore, the composition of inflow waters feeding Andean salars reflects a  
125 mixture from two main sources: (1) dilute waters produced by the alteration of volcanic  
126 rocks by meteoric waters and (2) brackish, highly concentrated waters derived from  
127 brine/salt recycling (Risacher et al., 2003 and references therein). The high rate of  
128 evaporation of these inflow waters in ponds and lakes increases the concentration of solutes  
129 and leads to the deposition of a sequence of minerals in the order of their increasing

130 solubility, following diverse evaporative pathways depending on the initial chemistry of  
131 inflow waters (Risacher and Fritz, 2009).

132  
133 With an area of ~120 km<sup>2</sup>, Laguna Pastos Grandes is one of the largest salars of the  
134 southern Altiplano (Risacher and Eugster, 1979). This salar lies at an elevation of 4450 m  
135 in a 50-km-long caldera dated at 2.89±0.01 Ma by <sup>40</sup>Ar/<sup>39</sup>Ar on sanidine (Salisbury et al.,  
136 2011) and is probably the remnant of a larger lake that once occupied the caldera moat (de  
137 Silva and Francis, 1991). The drainage basin (660 km<sup>2</sup>) is limited to the west by rhyolitic  
138 lava ridges up to an elevation of 5800 m, and to the east by rhyolitic ignimbrite ridges up  
139 to an elevation of 5000 m (Fig. 1b). Coalescent alluvial fans with thin pebbly soils and  
140 xerophytic vegetation surround the laguna. Laguna Pastos Grandes can be divided in two  
141 main domains previously identified by Ballivian and Risacher (1981) and Jones and Renaut  
142 (1994): the eastern domain corresponds to a playa environment characterized by gypsum  
143 and carbonate muds associated with ulexite (NaCaB<sub>5</sub>O<sub>6</sub>(OH)<sub>6</sub>), and the western domain  
144 corresponds to a vast 40-km<sup>2</sup> palustrine carbonate platform, highly fragmented through  
145 cryoturbation exposing underlying recent carbonates (muds to calcarenites). Over these  
146 recent carbonate deposits, a few ponds with a depth of no more than a decimeter are  
147 characterized by pisoliths and carbonate concretions reaching up to 20 cm (Fig. 2).  
148 Hydrothermal springs discharge over this platform producing important modern carbonate  
149 deposits (Bougeault et al., 2019).

### 150 3. Materials and Methods

#### 151 3.1 Water, gas and rock sampling

152 Nine water samples were collected during two sampling trips in January 2016 and  
153 March 2017, dry and wet seasons, respectively (Tables 1, 2). We thus consider our samples  
154 as representative of the two main climatic seasons in terms of rainfall. We collected seven  
155 samples of water from five thermal springs including one on the border of the laguna; two  
156 samples from cold streams; and one sample of brine from the southwestern part of the  
157 laguna (Fig. 2, Tables 1, 2). Water samples were filtered at 0.1 μm with a sterile acrylic  
158 filter (Sartorius Minisart<sup>®</sup>) fixed at the end of a 50 mL syringe and cation samples were  
159 acidified with HNO<sub>3</sub> in the field. The temperature and pH were measured on site at each  
160 collection point. The alkalinity was determined by HCl titration and Gran's plotting  
161 immediately after sampling and filtration in 2016 (Table 2) and for the 2017 samples, by  
162 end-point titration with H<sub>2</sub>SO<sub>4</sub> at the Total laboratory (France). Two samples of fresh snow  
163 and one sample of rainfall were also collected respectively in January 2016 and March  
164 2017 in order to constrain the meteoric sources of water in the area (Table A2).

165  
166 Four thermal springs named *La Salsa*, *La Rumba*, *El Ojo Verde* and *El Gigante*  
167 (Fig. 2) were selected for both water and gas sampling on the carbonate platform based on  
168 accessibility and high water-gas flux. *La Salsa*, *La Rumba* and *El Ojo Verde* springs contain  
169 bubbling sources of gas in water ponds whereas *El Gigante* is a dry source of gas (a mofet)  
170 away from the main water source. Gases were only collected in March 2017 in 100- and  
171 250-mL stainless-steel reservoirs and in four 12 mL Exetainer<sup>®</sup> vials, all previously  
172 evacuated to primary vacuum. To capture bubbling thermal spring gases, an inverted funnel  
173 connected to a rubber pipe was submerged in spring water and placed on top of the rising  
174 bubbles (Fig. A1). The other end of the pipe was then connected through a T-junction to a  
175 stainless-steel fitting ending in a septum (for sampling in an Exetainer<sup>®</sup>) and a stainless-

176 steel reservoir (for direct sampling) connected to a GA5000 gas detector (Scientific  
177 Instruments). Before collecting the gases accumulated in the funnel, the sampling system  
178 was completely flushed by the continuously outgassing bubbles to avoid air contamination.  
179 The O<sub>2</sub> level at the outlet of the sampling system was continuously monitored with the gas  
180 detector to ensure limited air contamination during sampling. The gas was collected when  
181 O<sub>2</sub> levels stabilized at the lowest level (typically below 2.0%).  
182

183 Five rock samples representative of the volcanic bedrock were also collected on the  
184 border of the laguna. These included two andesites, two dacites and one ignimbrite of  
185 rhyolitic composition (see location in Fig. 2).

## 186 **3.2 Analytical methods – Chemical compositions**

### 187 **Gas composition**

188 The composition of the gas was determined on the four samples (100, 112, 116, 117)  
189 collected in Exetainer<sup>®</sup> vials with a Varian 3800 high-resolution gas chromatograph (GC)  
190 at the IFPEN laboratory (Rueil-Malmaison, France). This GC is equipped with several  
191 columns, two thermal conductivity detectors (TCD) and one flame-ionization detector  
192 (FID) operating under He and N<sub>2</sub> as carrier gases. The quantification of H<sub>2</sub> and He was  
193 realized on one TCD with N<sub>2</sub> as the carrier gas, whereas CO<sub>2</sub>, N<sub>2</sub>, O<sub>2</sub> and CH<sub>4</sub> were  
194 analyzed using the other TCD with He as the carrier gas. Relative concentrations were  
195 calculated after the chromatographic response had been calibrated in partial pressure for  
196 each compound using the specific external standards "Air Liquide TM" and "Saphir".  
197 These standards are quality gas mixtures that include H<sub>2</sub>, He, N<sub>2</sub>, CO<sub>2</sub>, O<sub>2</sub>, CH<sub>4</sub>, C<sub>2</sub>H<sub>6</sub>,  
198 C<sub>3</sub>H<sub>8</sub>, n-C<sub>4</sub>H<sub>10</sub> and i-C<sub>4</sub>H<sub>10</sub> and are available in the laboratory at different concentrations  
199 to cover the specific sample compositions. Each analysis was bracketed with blanks.  
200 Results are given with a precision of ± 5 vol.% for O<sub>2</sub>, ±1.3 vol.% for CO<sub>2</sub>, ±3 vol.% for  
201 N<sub>2</sub> and ±0.1 vol.% for CH<sub>4</sub> based on repeated measurements of gas standards in similar  
202 concentrations.  
203

### 204 **Water composition**

205 All chemical analyses were carried out in the Total laboratories (Pau, CSTJF, France) using  
206 ion chromatography (Cl, Br and SO<sub>4</sub>); Inductively Coupled Plasma-Atomic Emission  
207 Spectroscopy (Li, B and Sr); Inductively Coupled Plasma-Mass Spectrometry (Ca and  
208 Mg); Flame Emission Spectrometry (Na, K, Ca and SiO<sub>2</sub>); and titration (alkalinity). The  
209 accuracy of the determination of major species was better than ± 5% and verified by  
210 repeated measurements of standard materials, namely Ion96-3 and LGC6020 for cations  
211 and anions, and pure Li and B standard solutions (Merck) for Li and B determinations.  
212 Saline samples were analyzed either after dilution (to minimize matrix effects during  
213 measurement) or by using the technique of adding a standard (to match the matrixes of the  
214 standard materials). The matrix effects were validated on at least three dilutions (500, 1000,  
215 2000).

## 216 **3.3 Analytical methods – Isotopic compositions**

### 217 **CO<sub>2</sub> gas**

218 The isotopic composition of the CO<sub>2</sub> was measured in samples contained in Exetainer<sup>®</sup>  
219 vials at the IFPEN laboratory using a MAT253 (Finnigan Mat-Thermo Fisher) triple  
220 collection mass spectrometer coupled to a gas chromatograph, operating with He as a  
221 carrier gas. The internal reference CO<sub>2</sub> gas was calibrated with the international gas

222 reference standards RM8562, RM8563 and RM8564 with  $\delta^{13}\text{C}_{\text{VPDB}}$  of  $-3.76 \pm 0.03 \text{ ‰}$ , -  
223  $41.56 \pm 0.04 \text{ ‰}$  and  $-10.45 \pm 0.03 \text{ ‰}$ , respectively (Verkouteren and Klinedinst, 2004). All  
224 the isotopic compositions given in this study are reported in the usual  $\delta$ -scale in ‰  
225 according to  $\delta_{\text{sample}} (\text{‰}) = \{(R_{\text{sample}}/R_{\text{standard}}) - 1\} \times 1000$ , where R is the  $^{13}\text{C}/^{12}\text{C}$  atomic ratio.  
226 The uncertainties on  $\delta^{13}\text{C}$  values are better than  $\pm 0.4 \text{ ‰}$  based on the external  
227 reproducibility of internal standards.

228

### 229 **N<sub>2</sub> gas**

230 The isotopic composition of N<sub>2</sub> was measured at the Institut de physique du globe de Paris  
231 (IPGP, France) on the gas captured in Exetainer<sup>®</sup> vials or stainless-steel cylinders. The N<sub>2</sub>  
232 was purified and isolated from other gases before being transferred to the IRMS dual-inlet  
233 mass spectrometer Delta + XP (Finnigan Mat-Thermo Fisher) for isotopic analyses. N<sub>2</sub>  
234 purification was performed using the high vacuum line ( $P < 10^{-5}$  mbar) described in Li et al.  
235 (2009). Purification starts with a cryogenic separation at liquid nitrogen temperature. The  
236 non-condensable gases, including N<sub>2</sub>, H<sub>2</sub>, O<sub>2</sub>, CH<sub>4</sub> and He, are inserted in the line and  
237 circulated using a mercury Toeppler pump through a CuO reactor maintained at 950 °C for  
238 30 minutes (and then cooled to 450 °C) to oxidize H<sub>2</sub> and CH<sub>4</sub>. The resulting CO<sub>2</sub> and H<sub>2</sub>O  
239 are cryogenically trapped at liquid-nitrogen boiling temperature. Excess O<sub>2</sub>, if any, is  
240 resorbed and the NO<sub>x</sub> that was potentially generated during the previous oxidation phase  
241 is reduced to N<sub>2</sub> by circulating the gases over a Cu reactor maintained at 600 °C. The  
242 purified N<sub>2</sub> and He are then collected with the mercury Toeppler pump and manometrically  
243 quantified before being transferred in vials for measurement using a dual-inlet IRMS Delta  
244 + XP. This instrument is calibrated by measuring an internal reference N<sub>2</sub> gas, itself  
245 calibrated against the air, the international reference standard for  $\delta^{15}\text{N}$  measurements,  
246 which has by definition an absolute value of  $\delta^{15}\text{N}_{\text{Air}} = 0 \text{ ‰}$ . We obtained a relative  
247 uncertainty on the  $\delta^{15}\text{N}$  better than  $\pm 0.5 \text{ ‰}$  taking into account the N<sub>2</sub> extraction process  
248 efficiency and the reproducibility on internal standards.

249 The CO<sub>2</sub> that was trapped using liquid nitrogen was then released at -140 °C, collected  
250 using a liquid N<sub>2</sub> trap and manometrically quantified before being transferred to vials for  
251 measurement using the dual-inlet IRMS Delta + XP.  $\delta^{13}\text{C}$  values compare well with those  
252 obtained by GC/C/IRMS at the IFPEN laboratory (Table A1).

253

### 254 **Noble gases**

255 Following the protocol of Moreira et al. (2018), noble gas isotopic compositions were  
256 measured in gas samples (100, 112, 116, 117) at IPGP using the Helix-SFT (Split Flight  
257 Tube, Thermo Instruments<sup>®</sup>). In brief the gas purification consists of several combustions:  
258 the first one with a Bulk Getter (SAES) heating system maintained at 400 °C for 5 minutes,  
259 followed by two 5-minute combustions at 800 °C each with titanium sponge. After  
260 purification, helium is separated from the other noble gases using activated charcoal at 30  
261 K, introduced into the Helix-SFT mass spectrometer and analyzed using peak jumping. <sup>3</sup>He  
262 is collected on the electron multiplier in pulse-counting mode whereas <sup>4</sup>He is analyzed on  
263 the Faraday cup and the signal is amplified using either 10<sup>11</sup> ohm or 10<sup>12</sup> ohm resistance  
264 depending on the signal. After the helium has been measured, neon is released from the  
265 cold trap at 70 K. Two cycles of neon isotope measurement are performed before neon is  
266 introduced to stabilize the magnet. For each cycle, <sup>20</sup>Ne is measured using a mass-scan  
267 instead of setting the magnet on the required field to measure <sup>20</sup>Ne (see Moreira et al., 2018  
268 for details). <sup>21</sup>Ne, <sup>22</sup>Ne, <sup>40</sup>Ar and CO<sub>2</sub> were measured for 10 seconds each using peak  
269 switching. Argon is partially desorbed at 130 K and transferred to charcoal at the

270 temperature of liquid nitrogen for 15 minutes. After the desorption of argon at room  
271 temperature from the charcoal trap, dilution(s) using a 1 L balloon is/are used to decrease  
272 the amount of argon introduced into the mass spectrometer.  $^{36}\text{Ar}$  and  $^{38}\text{Ar}$  are collected on  
273 the electron multiplier, whereas  $^{40}\text{Ar}$  is measured on the Faraday cup using  $10^{11}$  ohm  
274 resistance. All the data were corrected following the procedure of Moreira et al. (2018).  
275 For Ne and Ar, the standard is the atmosphere. The helium standard is a gas collected at  
276 the Irene thermal spring (Reunion island) with a  $^3\text{He}/^4\text{He}$  value of  $12.56 \pm 0.05 R_A$ . For the  
277 present study, blank corrections were negligible. Final uncertainties for the isotopic ratios  
278 in samples are  $\pm 0.1$  for R/Ra,  $\pm 0.06$  for  $^{20}\text{Ne}/^{22}\text{Ne}$ ,  $\pm 0.0005$  for  $^{21}\text{Ne}/^{22}\text{Ne}$ ,  $\pm 5$  for  $^{40}\text{Ar}/^{36}\text{Ar}$   
279 and correspond to the error propagation of the measured uncertainty, the blank correction,  
280 and the correction for mass discrimination.

281

### 282 **Water isotopes**

283 Oxygen and hydrogen isotope measurements were performed at BRGM's stable isotope  
284 laboratory by equilibrating 1 mL of water with gas mixtures of  $\text{H}_2$ -He and  $\text{CO}_2$ -He  
285 respectively for  $\delta^2\text{H}$  and  $\delta^{18}\text{O}$ , for one night and using a Finnigan MAT 252 mass  
286 spectrometer (Assayag et al., 2008). The external precision was  $\pm 0.1\text{‰}$  for  $\delta^{18}\text{O}$  and  $\pm$   
287  $0.8\text{‰}$  for  $\delta^2\text{H}$  vs. SMOW.

288

### 289 **Chlorine**

290 The chlorine stable isotope compositions were measured at the IPGP on gaseous  $\text{CH}_3\text{Cl}$   
291 that was prepared and purified with the method described in Godon et al. (2004). The  $\delta^{37}\text{Cl}$   
292 measurements were then performed on the dual-inlet IRMS Delta + XP. They are reported  
293 in Table A3 with the conventional  $\delta^{37}\text{Cl}$  notation in per mil variations relative to Standard  
294 Mean Ocean Chlorine (SMOC, Godon et al., 2004). During the course of this study, the  
295 external reproducibility of the seawater standard was  $0 \pm 0.04\text{‰}$  (1s, n = 18) as routinely  
296 obtained at IPGP for more than two decades now (Godon et al., 2004; Bonifacie et al.,  
297 2005; Giunta et al., 2015). Four pore fluid samples were measured twice. The mean  
298 difference value between duplicates was  $0.04\text{‰}$ .

299

### 300 **$\delta^7\text{Li}$ analysis**

301 In water samples, lithium isotopic compositions were measured using a Neptune  
302 Multi Collector ICP-MS (Thermo Fisher Scientific) at BRGM's stable isotope laboratory.  
303  $^7\text{Li}/^6\text{Li}$  ratios were normalized to the L-SVEC standard solution (NIST SRM 8545, Flesch  
304 et al., 1973) following the standard-sample bracketing method (see Millot et al., 2004 for  
305 more details). The uncertainties on  $\delta^7\text{Li}$  values are better than  $\pm 0.5\text{‰}$  ( $2\sigma$ ) based on the  
306 external reproducibility using internal standards (seawater IRMM BCR-403 and basalt JB-  
307 2).

308 In volcanic rocks, Li was separated from the matrix by ion-exchange  
309 chromatography using the method described in detail by Dellinger et al. (2015). In brief,  
310 after digestion, a sample aliquot was loaded onto a column filled with AG50-X12 resin and  
311 the Li was eluted in HCl 0.2 N. The Li isotopic composition was measured by MC-ICP-  
312 MS Neptune (Thermo Scientific, Bremen) at IPGP using an APEX desolvating system and  
313 at typical Li concentrations of 20–30 ppb. Each sample was successively measured three  
314 times within a standard-sample bracketing (SSB) sequence, yielding five  $\delta^7\text{Li}$  values from  
315 which an average value was derived. Data were corrected for the background intensities  
316 recorded before each bracketing standard and each sample. The intensity of the background  
317 was no more than 0.5–1% of the sample intensity. The overall reproducibility and accuracy

318 of the procedure (including solid sample digestion and Li separation) was checked by  
319 measurement of the basalt reference material BHVO-2 ( $\delta^7\text{Li} = 4.23 \pm 0.83\%$ ; Ryu et al.,  
320 2014). The external error ( $2\sigma$ ) was better than 0.5%. Finally, the concentration of the total  
321 procedural blank (acid digestion and column chemistry) was assessed to be less than 0.05  
322 ng, i.e., insignificant compared with the amount of Li in the samples. The results are given  
323 in Table 4.

324

### 325 $\delta^{11}\text{B}$ analysis

326 In water samples, boron isotopic compositions were determined on a Finnigan  
327 MAT 261 solid source mass spectrometer in a dynamic mode at BRGM's stable isotope  
328 laboratory. For these samples, water volumes corresponding to a mass of 10  $\mu\text{g}$  of B  
329 underwent a two-step chemical purification using Amberlite IRA-743 selective resin  
330 according to a method adapted from Gaillardet and Allègre (1995). The uncertainties on  
331  $\delta^{11}\text{B}$  values are better than  $\pm 0.3\%$  ( $2\sigma$ ) based on the external reproducibility using the  
332 internal standard NBS951 ( $\delta^{11}\text{B} = 4.05398 \pm 0.00105\%$ ).

333 Rock samples were dissolved by alkali fusion and B was extracted following the procedure  
334 of Chetelat et al. (2009). 50 mg of finely powdered sample were admixed with 300 mg of  
335 ultra-pure  $\text{K}_2\text{CO}_3$  in a Pt crucible and melted in a muffle furnace at 950  $^\circ\text{C}$  for 15 minutes.  
336 The pellet was taken up in 3 mL of 0.5  $\text{HNO}_3$  and added to a 50 mL vial filled with 20 mL  
337  $\text{H}_2\text{O}$ . An additional 1-2 mL of 0.5N  $\text{HNO}_3$  were added until complete dissolution. The final  
338 pH was adjusted to pH 1.7 with 3N  $\text{HNO}_3$ , and 7 mL of this solution were passed through  
339 2 mL of the cation exchange resin AG 50W-X8 to extract most of the cationic load. The  
340 recovered solution was adjusted to pH 8-9 with distilled 4N  $\text{NH}_4\text{OH}$  and B was extracted  
341 on Amberlite IRA-743 resin (adapted from Lemarchand et al., 2002) in two steps: the first  
342 step consisted of extraction on a column loaded with 300  $\mu\text{L}$  of resin and the second step  
343 of purification (after adjustment to pH 8-9 again) on a column filled with 50  $\mu\text{L}$  of the  
344 resin. Boron isotope ratios were determined by MC-ICP-MS with a direct injection  
345 nebulizer (d- DIHEN; Louvat et al., 2014) at IPGP with a  $2\sigma$  reproducibility between 0.05  
346 and 0.3%.  $^{11}\text{B}/^{10}\text{B}$  values are expressed relative to the boric acid standard NBS 951 (NIST).  
347 The results are given in Table 4.

348

### 349 $^{87}\text{Sr}/^{86}\text{Sr}$ measurement

350 In water samples, chemical purification of Sr ( $\sim 3 \mu\text{g}$ ) was done using an ion-  
351 exchange column (Sr-Spec) before mass analysis according to a method adapted from Pin  
352 and Bassin (1992) with total blank  $< 1 \text{ ng}$  for the entire chemical procedure. After chemical  
353 separation, around 150 ng of Sr were loaded onto a tungsten filament with tantalum  
354 activator and analyzed with a Finnigan MAT 262 multi-collector mass spectrometer at  
355 BRGM's stable isotope laboratory. The  $^{87}\text{Sr}/^{86}\text{Sr}$  values were normalized to the certified  
356 value of the NBS987 standard 0.710240. An average internal precision of  $\pm 10 \text{ ppm}$  ( $2\sigma$ )  
357 was obtained and the reproducibility of the  $^{87}\text{Sr}/^{86}\text{Sr}$  ratio measurements was verified by  
358 repeated analysis of the NBS987 standard ( $^{87}\text{Sr}/^{86}\text{Sr} = 0.710243 \pm 10, 2\sigma$ ).

359 After total evaporation of  $\sim 0.2 \text{ mL}$  of rock sample digestion solutions, the  
360 remaining solid was retaken with 0.1 mL of  $\text{HNO}_3$  3N and loaded onto a Sr-SPEC  
361 (Eichrom) resin chromatography column to separate ca. 200 ng of Sr (Pin and Bassin,  
362 1992). The Sr isotopic composition was measured by MC-ICP-MS at the IPGP. The mass  
363 discrimination was corrected using the invariant ratio  $^{88}\text{Sr}/^{86}\text{Sr}$  (0.1194). Accuracy and  
364 reproducibility were verified by repeated analysis of the NBS standard SRM 987 ( $^{87}\text{Sr}/^{86}\text{Sr}$   
365  $= 0.710250 \pm 0.0000025$ ). The results are given in Table 4.



366

### 3.5 PHREEQC modeling

367 The PHREEQC software, version 3 (Parkhurst and Appelo, 2013) was applied to compute  
 368 aqueous speciation and fluid-mineral equilibria using the “thermoddem v1.10 06jun2017”  
 369 thermodynamic database (website <http://thermoddem.brgm.fr/>; Blanc et al., 2012).

## 370 4. Results

371

### 4.1 Gas molecular and noble gases composition

372 *Table 1. Analytical results of the gas sampled in 2017: bubbling gas from La Salsa, La*  
 373 *Rumba and El Ojo Verde spring sources and dry gas from El Gigante gas source.  $\delta^{15}\text{N}$  and*  
 374  *$\delta^{13}\text{C}$  values are averaged from multiple measurements ( $n=2-6$ ) except for sample*  
 375 *PG17\_116, which was analyzed only once for  $\delta^{15}\text{N}$  (see Table A1 for detailed nitrogen and*  
 376 *carbon isotopic analyses). See text for calculations of atmospheric  $\text{N}_2$  proportion,  $\delta^{15}\text{N}$*   
 377 *correction from atmospheric contribution and modeling results.*

Sample no.	PG17_100	PG17_112	PG17_116	PG17_117
Sample location	La Salsa	La Rumba	El Gigante	El Ojo Verde
Latitude (°S)	21.619349	21.638776	21.64819	21.651306
Longitude (°W)	67.848462	67.852883	67.848736	67.840695
Temperature (°C)	43.4	44.6	41.5	36.2
Major composition (vol.%)				
CO <sub>2</sub>	74.7	66.2	86.0	38.4
CH <sub>4</sub>	0.04	0.03	0.00	0.07
O <sub>2</sub>	3.36	2.01	1.63	4.76
N <sub>2</sub>	21.8	32.0	12.4	56.4
% N <sub>2</sub>	57.3	23.4	49.1	31.5
Isotopic composition (‰)				
$\delta^{13}\text{C}$ ( $\pm 0.1\text{‰}$ , $2\sigma$ )	-11.2	-11.2	-11.2	-11.0
$\delta^{15}\text{N}$ ( $\pm 0.5\text{‰}$ , $2\sigma$ )	2.7	1.8	1.6	2.3
$\delta^{15}\text{N}_{\text{primary}}$	6.4	2.3	3.1	3.4
Noble gases (ppm)				
<sup>4</sup> He	337	517	109	814
<sup>20</sup> Ne	0.561	1.498	0.425	2.033
<sup>36</sup> Ar	7.089	12.865	3.575	12.169
<sup>40</sup> Ar/ <sup>36</sup> Ar	298	288	283	288
R <sub>C</sub> /R <sub>A</sub>	3.68	3.84	3.81	3.86
Mantle He (%)	45.4	47.3	47.1	47.6
CO <sub>2</sub> / <sup>3</sup> He <sub>surface</sub>	4.35*10 <sup>8</sup>	2.42*10 <sup>8</sup>	1.51*10 <sup>9</sup>	8.85*10 <sup>7</sup>
Modeling				
CO <sub>2</sub> / <sup>3</sup> He <sub>before degassing</sub>	1.2*10 <sup>8</sup>	9.6*10 <sup>8</sup>	2.9*10 <sup>9</sup>	4.7*10 <sup>8</sup>
CO <sub>2</sub> exsolution (%)	36	23	49	17

378

379 The gas from thermal springs is mainly composed of CO<sub>2</sub> (38.4 to 86 vol. %) and N<sub>2</sub> (12.4  
 380 to 56.4 vol. %) with minor amounts of O<sub>2</sub> (1.63 to 4.76 vol. %) and negligible traces of  
 381 CH<sub>4</sub> (< 0.07 vol. %; Table 1, Fig. 2). No H<sub>2</sub> and H<sub>2</sub>S were detected. If we assume that O<sub>2</sub>  
 382 is derived from atmospheric contamination during sampling or natural diffusion into the  
 383 thermal spring from the surface, we can calculate a contribution of associated atmospheric  
 384 N<sub>2</sub> up to 57.3% of the total N<sub>2</sub> (Table 1). The air-normalized abundances of the

385 Atmosphere-Derived Noble Gases (ADNG:  $^{20}\text{Ne}$  and  $^{36}\text{Ar}$ ) display depleted values  
 386 compared with air that follow the composition of the Air Saturated Water (ASW; Fig. 3).  
 387 In contrast,  $^4\text{He}$  is found in high proportions, from 109 to 814 ppm, displaying a high  
 388  $^3\text{He}/^4\text{He}$  value normalized to air ( $R_C/R_A$ ) of  $3.79 \pm 0.08$  on average (with  $(^3\text{He}/^4\text{He})_{\text{air}} =$   
 389  $1.4 \times 10^{-6}$ ; Table 1). This value indicates a high mantle contribution (Sano and Marty, 1995,  
 390 see discussion).

391

## 392 4.2 Gas C and N isotope compositions

393

394 The  $\text{CO}_2$  gas sampled from thermal springs shows homogeneous  $\delta^{13}\text{C}$  values with an  
 395 average of  $-11.1 \pm 0.1\text{‰}$  (Table 1, A1). In contrast, the isotopic composition of  $\text{N}_2$  ( $\delta^{15}\text{N}$ )  
 396 is more variable and ranges between 1.6 and  $2.7 \pm 0.5\text{‰}$ . Nitrogen isotope measurements  
 397 of sample PG17\_112 were performed on gases sampled in both Exetainers<sup>®</sup> and stainless-  
 398 steel tubes to ensure a good reproducibility of the results, regardless of the container used  
 399 (Table A1). Considering an atmospheric contamination of up to 57.3% for  $\text{N}_2$ , we can  
 400 estimate the primary  $\delta^{15}\text{N}$  value by isotopic mass balance as follows:

$$401 \delta^{15}\text{N}_{\text{measured}} = \delta^{15}\text{N}_{\text{atm}} \cdot \%_{\text{atm}} + \delta^{15}\text{N}_{\text{primary}} \cdot (1 - \%_{\text{atm}})$$

402 With atmospheric contamination  $\%_{\text{atm}}$  up to 0.573 and  $\delta^{15}\text{N}_{\text{atm}} = 0\text{‰}$ , we obtain a  
 403 maximum  $\delta^{15}\text{N}_{\text{primary}}$  of 6.4‰ (Table 1). We thus consider the measured values as  
 404 minimal values.

405

## 406 4.3 Isotopic composition of water

407

408 *Table 2. Chemical and isotopic data for Laguna Pastos Grandes waters. NICB:*  
 409 *Normalized Ionic Charge Balance.*

Sample no.	PG17-117	PG17-112	PG17-100	PG1_1	MV_1	PGS_1	PG17_99	SP_3	LS_4
Sampling trip	2017	2017	2017	2016	2016	2016	2017	2016	2016
Name	El Ojo Verde spring	La Rumba spring	La Salsa spring	La Salsa spring	El Gigante spring	Piedmont spring	Stream	Stream	Lake brine
Lat. (°S)	21.651306	21.638776	21.619349	21.61934	21.64865	21.61996	21.60764	21.69665	21.69552
Lg. (°W)	67.840695	67.852883	67.848462	67.84842	67.84866	67.85628	67.75753	67.8098	67.80927
T (°C)	36.2	44.6	43.4	42.2	45.7	32.4	17.3	16.4	24.5
pH	6.41	5.99	6.90	6.42	6.20	6.35	9.15	7.99	7.39
Alkalinity on site				10.7	8.91	4.35		0.78	
Chemical composition (mM)									
Na	232	137	173	220	251	23.7	0.57	1.17	3924
K	12.9	8.7	12.5	13.4	16.6	1.8	0.14	0.36	131
Ca	10.9	6.5	10.1	11.4	12.8	0.7	0.17	0.37	59.7
Mg	5.8	2.8	5.2	5.4	6.0	0.4	0.13	0.18	54.6
Alkalinity	7.4	5.3	7.4	7.4	8.9	1.8	0.90	0.79	10.9
SO <sub>4</sub>	2.9	2.3	2.3	2.9	4.2	0.8	0.04	0.22	39.5
Cl	278	173	197	258	291	25.5	0.73	1.52	4375
Li	11.1	6.6	9.9	7.7	9.6	0.8	0.02	0.25	74.8
Sr	0.11	0.06	0.11	0.11	0.15	0.01	0.001	0.003	1.03
B	3.6	2.2	3.3	3.2	4.7	0.5	0.04	0.08	28.6
Br	0.073	0.046	0.069	0.060	0.070	0.006	0.006	0.006	0.426
SiO <sub>2</sub> *	116	101	116	155	152	101	36	60	60
Salinity**	16.2	10.1	11.5	15.1	17.0	1.49	0.04	0.09	256
NICB (%)	-1.3	-7.5	6.9	0.7	2.2	-3.1	-26.4	3.0	-2.9
pCO <sub>2</sub> (mbar)***	141	309	60.3	110.0	389.0	61.7	0.03	0.5	10.5
Isotopic compositions (‰ ±2s)									

$\delta^2\text{H}$ ( $\pm 0.8$ )	-92.2	-96.7	-93.9	-93.8	-92.5	-104.2	-99.4	-104.7	7.6
$\delta^{18}\text{O}_{\text{H}_2\text{O}}$ ( $\pm 0.1$ )	-11.4	-12.4	-11.8	-11.7	-11.4	-14.2	-13.1	-13.2	3.3
$\delta^7\text{Li}$	5.2 $\pm$ 0.1	5.6 $\pm$ 0.1	3.8 $\pm$ 0.1	3.6 $\pm$ 0.1	4.0 $\pm$ 0.2	2.6 $\pm$ 0.2	4.0 $\pm$ 0.2	10.9 $\pm$ 0.1	3.9 $\pm$ 0.3
$\delta^{11}\text{B}$	-4.4 $\pm$ 0.1	-5.0 $\pm$ 0.1	-4.9 $\pm$ 0.2	-4.3 $\pm$ 0.3	-6.7 $\pm$ 0.3	-6.0 $\pm$ 0.3		0.0 $\pm$ 0.3	-7.2 $\pm$ 0.3
$^{87}\text{Sr}/^{86}\text{Sr}$	0.708384	0.708412	0.708398	0.708396	0.708402	0.708354	0.707950	0.707646	0.708327
$2\text{S}_{\text{m}}$	0.000005	0.000006	0.000010	0.000007	0.000006	0.000006	0.000010	0.000007	0.000007

410 \*mg/L; \*\*g/L; \*\*\*calculated with PHREEQC based on water chemistry

411

412 Spring waters exhibit a narrow range for  $\delta^{18}\text{O}$  (-14.2 to -11.4‰) and  $\delta^2\text{H}$  (-104.2 to -  
413 92.2‰) and slightly more enriched in  $^{18}\text{O}$  and  $^2\text{H}$  than streams (with  $\delta^{18}\text{O} \sim -13.2$ ‰ and -  
414  $104.7 < \delta^2\text{H} < -99.4$ ‰; Fig. 4, Table 2). They are on the regional Ground and Spring Water  
415 Line (LGSWL;  $\delta^2\text{H} = 7.99 \times \delta^{18}\text{O} + 0.3$ ;  $n = 44$ ) established by Fritz et al. (1981) and  
416 Rissmann et al. (2015) to the right of the Local Meteoric Water Line (LMWL) defined for  
417 modern precipitation in the Chilean and Bolivian Altiplano at altitudes of 2800 to 5700 m:  
418  $\delta^2\text{H} = 8.15 \times \delta^{18}\text{O} + 15.3$  (Chaffaut et al., 1998). Both streams and springs define a trend  
419 modeled by the following equation:  $\delta^2\text{H} = 4.29 \times \delta^{18}\text{O} + 43.8$  ( $R^2 = 95\%$ ,  $n = 8$ ; Fig. 4b)  
420 with more positive  $\delta^{18}\text{O}$  and  $\delta^2\text{H}$  values than rainfall collected at the altitude of the aquifer  
421 system (i.e., at an altitude of 4500 m) during the wet season in March 2017. Two samples  
422 of snow collected during the dry season in January 2016 show more positive  $\delta^{18}\text{O}$  and  $\delta^2\text{H}$   
423 values than rainfall and fall to the left of the LMWL trend (Table A2). The Piedmont  
424 thermal spring, located on the border of the laguna, is shifted from the other springs toward  
425 more negative  $\delta^{18}\text{O}$  and  $\delta^2\text{H}$  values. In the southeastern part of Laguna Pastos Grandes, the  
426 brine sampled from the southeastern lake (LS4 sample) is enriched in both  $^{18}\text{O}$  and  $^2\text{H}$   
427 compared with the different inlet waters and shows even greater  $\delta^{18}\text{O}$  and  $\delta^2\text{H}$  values than  
428 other Andean salars on average (Fig. 4, Table A2).

429

#### 430 4.4 Geothermometry

431

432 Table 3. Estimated equilibrium temperatures ( $^{\circ}\text{C}$ ) for hydrothermal sources obtained with  
433 different geothermometers.

Geothermometer	PG17_117	PG17_112	PG17_100	PG1_1	MV_1	PGS_1
$\text{SiO}_2$ (Verma and Santoyo, 1997)	145	138	145	163	162	138
Na/K/Ca – Mg (Fournier and Potter, 1979)	177	144	169	167	171	107
Na/K (Verma and Santoyo, 1997)	215	226	237	222	230	240
Na/K (Santoyo and Diaz-Gonzalez, 2010)	188	202	216	197	221	207
Na/Li (Fouillac and Michard, 1981)	315	316	344	272	283	268
Na/Li (modified by Sanjuan et al., 2014)	264	264	285	230	239	226
Na/Li (Verma and Santoyo, 1997)	323	324	351	280	292	276
Na/Li (Kharaka et al., 1982)	334	335	353	304	312	301
Na/Li (modified by Sanjuan et al., 2014)	336	337	355	306	314	303
Mg/Li (Kharaka and Mariner, 1989)	199	193	197	185	192	151

434

435 The thermal waters associated with gases reach the surface at up to 46  $^{\circ}\text{C}$ , which is among  
436 the highest temperatures recorded in the Altiplano salars (Risacher and Fritz, 1991; Spiro  
437 et al., 1997). Considering the concentrations of some soluble elements (Si, Na, K, Ca, Mg,  
438 Li) in the thermal springs, it is possible to calculate temperatures of the fluids based on  
439 empirical, semi-empirical and experimental relations derived from known or unknown  
440 equilibrium relations between water and minerals taking place in the geothermal reservoirs  
441 (Sanjuan et al., 2014 and references therein). For example, the silica concentration of our

442 samples is fairly uniform within the range of 101 to 154 mg/l (Table 2). Applying the quartz  
443 geothermometer described in Kharaka and Mariner (1989), Verma and Santoyo (1995,  
444 1997) estimated equilibrium temperatures of spring water with the rocks of a deep reservoir  
445 up to  $163 \pm 3$  °C (assuming no steam loss; Table 3) with a mean of 149 °C. This estimate  
446 decreases by less than 9 °C if we consider adiabatic cooling of the fluid by steam loss after  
447 leaving the reservoir (Kharaka and Mariner, 1989). This small shift supports the idea that  
448 the original silica concentration in the fluid was only slightly affected by boiling and/or  
449 dilution (Cortecchi et al., 2005). However, considering the contrast in temperature between  
450 the surface and the deep reservoir, a precipitation of silica during the cooling of the water  
451 as it ascends to the surface is easy to hypothesize. This loss will minimize the  
452 geothermometer based on the silica concentration. The Na-K-Ca geothermometer yields  
453 similar estimates (156 °C) with a maximum shift of  $\pm 30$  °C when the Mg correction of  
454 Fournier and Potter (1979) is applied. However, this geothermometer is calibrated on  
455 silicates and can also be affected by a precipitation of silicates during the cooling of the  
456 thermal water.

457  
458 The Na-Li geothermometer gives much higher estimates (around 300 °C) regardless of the  
459 equation used (Fouillac and Michard, 1981; Kharaka et al., 1982; Verma and Santoyo,  
460 1993, 1997). Using a larger dataset than in the original articles, Sanjuan et al. (2014)  
461 modified the equations of Kharaka et al. (1982) and Fouillac and Michard (1981). These  
462 corrections do not modify the results for the Kharaka et al. equation (mean value 325 °C)  
463 but decrease the values obtained with the Fouillac and Michard equation (mean value 251  
464 °C) by 50 °C. The Li-Mg geothermometer (Kharaka and Mariner, 1989) yields lower  
465 values ( $\sim 186$  °C on average; Table 3) than the Na-Li geothermometer. The discrepancies  
466 observed between the geothermometers using Li can be explained by the high  
467 concentrations of Li in our samples. The  $\text{Log}(\text{Na}/\text{Li})$  values obtained for the thermal  
468 springs of Laguna Pastos Grandes are between 1.24 and 1.47 whereas the values used by  
469 Sanjuan et al. (2014) for their calibrations are never lower than 2.00. Consequently, our  
470 data are not in the range of calibration of the equations and if the correlations cannot be  
471 extended linearly, the uncertainties on the calculated temperatures will be high.

472  
473 The geothermometer based on Li isotopes was also tested as it is independent from the Li  
474 concentration. This geothermometer was calibrated experimentally on springs from the  
475 Guadeloupe and Martinique volcanic arcs (Millot et al., 2010). It relies on the fact that Li  
476 isotopic fractionation ( $\Delta_{\text{solution-solid}}$ ) between solution and basalt is strongly temperature  
477 dependent with, for example, values of +19.4‰ at 25 °C to 6.7‰ at 250 °C. Considering  
478 the  $\delta^7\text{Li}$  mean value of  $4.44 \pm 0.90$ ‰ for thermal springs and using the values for rhyolitic  
479 ignimbrite, dacite and andesite in the area that are reported in Table 4, we obtained a  
480 fractionation  $\Delta_{\text{solution-solid}}$  of 8, 10 and 12‰, respectively. This fractionation is low and can  
481 be related to hot temperatures ( $> 125$  °C). Knowing that the Central Andes Ignimbrites are  
482 a 50:50 mixture of mantle-derived basalts and of regional crust (de Silva and Kay, 2018),  
483 we can hypothesize that the behavior of Li in these rocks and in the altered products is not  
484 very different from that in the andesite of Guadeloupe. In this case, the calibration  
485 temperature of Millot et al. (2010) would give a temperature of  $200 \pm 25$  °C. The Na-K  
486 geothermometer yields similar estimates of  $228 \pm 9$  °C with the equation of Verma and  
487 Santoyo (1997) and  $205 \pm 12$  °C with that of Santoyo and Diaz-Gonzalez (2010).  
488

489 In summary, the geothermometers used in this study yield equilibrium temperatures of  
490 spring water with the rocks of a deep reservoir between 150 and 325 °C. The first value  
491 (given by silica geothermometer) is too low and reflects a probable precipitation of silica  
492 during thermal water cooling. The highest value (given by Na/Li geothermometers) is  
493 uncertain because Li concentrations in the fluids are too high for the available calibrations.  
494 We thus retain the range of temperature obtained using  $\delta^7\text{Li}$  and Na/K geothermometers,  
495 i.e., between 200 and 250 °C, as the maximum temperature encountered by the infiltrated  
496 water through the faults of the Pastos Grandes caldera. This temperature is compatible with  
497 a depth of 3 km, which corresponds to the top of an ancient pre-eruptive magma reservoir  
498 of the volcano (de Silva and Kay, 2018).

499

500

#### 4.5 Chemical composition of the water

501

502 As extensively demonstrated in previous papers (Stallard and Edmond, 1981; Roche et al.,  
503 1991; Moquet et al., 2011), we assumed the atmospheric contribution to groundwater  
504 chemistry as negligible in this region and did not correct the data from this contribution.  
505 Our results of elemental concentrations obtained in Laguna Pastos Grandes are represented  
506 and interpreted together with those from previous studies of this laguna (Ballivian and  
507 Risacher, 1981; Hurlbert and Chang, 1984; Risacher and Fritz, 1991; Jones and Renaut,  
508 1994). Spring waters are saline with an average salinity of ~14 g/L compared with the  
509 streams with 0.09 g/L of maximum salinity and show homogeneous  $\delta^{37}\text{Cl}$  values of  
510  $0.25 \pm 0.03\text{‰}$  (n=12; Table A3). The Piedmont spring is the only exception with a relatively  
511 low salinity of 1.9 g/L. The brines from the southeastern part of the laguna are more saline  
512 than the water sources (256 g/L; Table 2).

513 Most of the waters show charge balances better than  $\pm 8\%$  (Table 2), which denote a  
514 negligible influence of potential organic charges to the ionic balance. One sample of stream  
515 water shows a charge balance of -26% corresponding to an anion excess of 0.41 mM.

516 The Schoeller diagram (Fig. 5a) shows that streams and springs have different  
517 compositions. Sodium and chloride are the dominant ions in spring waters, with average  
518 concentrations of 173 and 203 mM, respectively. With a Ca:Mg molar ratio ranging from  
519 1.9 to 2.4, they are all Ca dominant relative to Mg. Hydrothermal springs show similar  
520 relative ion concentrations suggesting that a common origin and common processes  
521 constrained the chemistry of their major elements (Fig. 5a). Their Ca:alkalinity molar ratio  
522 is favorable to the precipitation of calcite (with a ratio of almost one Ca for two C).  
523 Compared with the hydrothermal springs, the Piedmont spring is diluted by surface waters.  
524 As for the laguna brine, it presents relative ion concentrations similar to those of the  
525 hydrothermal springs but with lower alkalinity. Its Ca:alkalinity ratio is not favorable to  
526 the precipitation of calcite (Fig. 5b).

527

#### 4.6 $\delta^7\text{Li}$ , $\delta^{11}\text{B}$ and $^{87}\text{Sr}/^{86}\text{Sr}$ in waters compared with surrounding rocks

528

529

530

531

532

533

534 Table 4. Summary of chemical and isotopic data available for dacites, andesites and  
 535 ignimbrites from Laguna Pastos Grandes. Data in italic are from previous studies cited in  
 536 parentheses.

Rock type	Ca/Na	Mg/Na	Li (ppm) ±0.3 1SD	$\delta^7\text{Li}$ (‰)	B (ppm) ±0.3 1SD	$\delta^{11}\text{B}$ (‰)	Sr (ppm) ±3 1SD	$^{87}\text{Sr}/^{86}\text{Sr}$
Ignimbrite	0.61	0.30	66.9	-3.33±0.47	54	-7.79±0.21	330	0.725764
Dacite 1	0.70	0.45	147.4	-5.82±0.12	60	-14.88±0.21	351	0.707906
Dacite 2	0.87	0.36	80.2	-5.43±0.35	30	-13.70±0.15	464	0.706951
Andesite 1	1.69	1.50	279.7	-5.11±0.38	144	-13.57±0.09	690	0.705835
Andesite 2	2.13	1.61	147.8	-9.22±0.15	116	-13.89±0.10	706	0.706206
<i>Ignimbrite (Kaiser, 2014)</i>								<i>0.708173</i>
<i>Ignimbrite (Kaiser, 2014)</i>								<i>0.708040</i>
<i>Cenomanian-Turonian carbonates (McArthur et al., 1994)</i>								<i>0.707298-0.707428</i>
<i>Modern marine evaporites (Pierret et al., 2001)</i>								<i>0.708940</i>

537

538 Thermal springs show homogeneous  $^{87}\text{Sr}/^{86}\text{Sr}$  values slightly more radiogenic than cold  
 539 streams with average values of  $0.70839\pm 0.00002$  and  $0.70780\pm 0.00021$ , respectively. In  
 540 the eastern part of the laguna, the perennial lake has an  $^{87}\text{Sr}/^{86}\text{Sr}$  value of 0.70833, which  
 541 is slightly lower than thermal spring water values. As expected, all waters are within the  
 542 range reported for dacites ( $0.70890\pm 0.00238$ ; Cortecchi et al., 2005) and andesites  
 543 ( $0.70763\pm 0.00161$ ; Cortecchi et al., 2005) of the Andean Central Volcanic Zone. Our dataset  
 544 is also compared with andesites, dacites and rhyolitic ignimbrites sampled in the vicinity  
 545 of Laguna Pastos Grandes (Table 4). Sr isotope ratios of streams are between those of  
 546 Pastos Grandes ignimbrites and dacites, whereas springs and brines show compositions  
 547 similar to ignimbrites (Fig. 6a). The  $^{87}\text{Sr}/^{86}\text{Sr}$  value of Cenomanian-Turonian marine  
 548 carbonates, considered as the last open marine period in the central Andes (Deconinck et  
 549 al., 2000), is much lower than the values of the thermal springs (with  $^{87}\text{Sr}/^{86}\text{Sr} = 0.7073$ -  
 550  $0.7074$ ; McArthur et al., 1994).

551 Similarly, the boron and lithium isotopic compositions of collected waters are clearly  
 552 different from seawater composition ( $\delta^{11}\text{B} = 39.6\%$  and  $\delta^7\text{Li} = 31.0\%$ ; Boschetti et al.,  
 553 2017).  $\delta^{11}\text{B}$  and  $\delta^7\text{Li}$  values increase between rock and water samples in the following  
 554 order: volcanic rocks < hydrothermal springs = lake brines < surface runoff. Pastos  
 555 Grandes' thermal waters and brine show homogeneous  $\delta^{11}\text{B}$  and  $\delta^7\text{Li}$  values around -5.5  
 556 and +4.1 ‰, respectively (Fig. 6b). In comparison, one stream displays more positive  
 557 values for both  $\delta^{11}\text{B}$  and  $\delta^7\text{Li}$ , at 0 and 10.9‰, respectively, whereas surrounding volcanic  
 558 rocks are more negative, with  $\delta^{11}\text{B}$  between -14.9 and -7.8‰ and  $\delta^7\text{Li}$  between -9.2 and -  
 559 3.3‰ (Fig. 6b; Table 4). In the studied area, volcanic rocks have high Li and B  
 560 concentrations (67–280 ppm of Li and 30–144 ppm of B) and isotopic compositions  
 561 depleted in  $^7\text{Li}$  and  $^{11}\text{B}$  compared with the range of values for the Andean volcanic arc: 3-  
 562 9 ppm of Li with  $-6.4 < \delta^7\text{Li} < -4.5\%$  (Chan et al., 2002) and 6-60 ppm of B with  $-7 < \delta^{11}\text{B}$

563 < +4‰ (Rosner et al., 2003). Our boron isotopic compositions are similar to the continental  
 564 crust ( $\delta^{11}\text{B}$  usually between -15 and -10‰; Chaussidon and Albarède, 1992).

565 **4.7 Thermodynamic model**

566 We compared the average spring water composition and the water chemistry obtained  
 567 using PHREEQC modeling of the alteration of the volcanic bedrock at 200-250 °C with a  
 568 CO<sub>2</sub> partial pressure between 10 and 100 bar (typical of CO<sub>2</sub>-rich geothermal systems;  
 569 Lowenstern, 2001). The objective was to determine if the observed concentrations of major  
 570 cations (Ca, Mg, K, Na and Si) can be reached by dissolution of the volcanic rocks (Table  
 571 A4, see Appendix for the PHREEQC model) without input of ancient marine sediments.  
 572 For the bedrock's mineral composition, we selected from the minerals available in the  
 573 Thermoddem database those closer to the mineralogy observed in the volcanic rocks  
 574 surrounding Laguna Pastos Grandes (details in Appendix):

- 575 – Albite for the source of Na
- 576 – Anorthite for Ca
- 577 – Pargasite for Mg
- 578 – Quartz for Si
- 579 – Sanidine for K

580 In all the models tested, Si concentration and DIC are higher than in the spring water. For  
 581 Ca, Mg, K and Na concentrations, the best result is obtained at 225 °C with 20 bar of CO<sub>2</sub>  
 582 (SI=1.3; Fig. 7). To adjust the Cl concentration in the water, we tried different Cl sources:  
 583 pure magmatic Cl<sub>2</sub>(g) or halite. The modeling results were not conclusive with pure  
 584 magmatic Cl<sub>2</sub>(g) but consistent with halite, suggesting that the salinity of the spring water  
 585 is provided by the dissolution of halite. Because halite is commonly associated with  
 586 gypsum in the sedimentary record of the Andean region, we also added anhydrite to the  
 587 bedrock composition in the model. Despite this, the main Ca source in the spring waters  
 588 remains the anorthite (Table A4). All the minerals were considered in the calculation as  
 589 infinite reservoirs except for halite, which was fixed by the average Cl concentration in the  
 590 spring water (239 mM).

591 **5. Discussion**

592 *Table 5. Comparison of Laguna Pastos Grandes characteristics with Chilean and Bolivian*  
 593 *salars. Data from this study and Hoke et al., 1994; Spiro et al., 1997; Risacher et al., 2003,*  
 594 *2011; Risacher and Fritz, 1991, 2009. ul: ulexite; hal: halite; gyps: gypsum; mirab:*  
 595 *mirabilite. \*Previous data TDS: Total Dissolved Solids*

	<b>Laguna Pastos Grandes</b>	<b>Chilean salars</b>	<b>Bolivian salars</b>
Location	Bolivian Altiplano	Western Cordillera	Bolivian Altiplano
Basement	Dacite-Andesite- Rhyolitic Ignimbrite	Rhyolitic ignimbrite Andesite	Andesite Rhyodacite
Altitude	4450 m	3400-4300 m	4100-4600 m
Surface	130 km <sup>2</sup>	0.03-400 km <sup>2</sup>	0.03-500 km <sup>2</sup>
Potential evaporation	1400 mm/year	1000-2000 mm/year	1000-1500 mm/year
Precipitation	100 mm/year	40-380 mm/year	50-150 mm/year
Mean temperature	5 °C	0 °C	5-10 °C
Morphology	Playa lake	Mainly playa lakes	Mainly playa lakes
Salinity	256 g/l	1.2-365 g/l	0.4-348 g/l
Brine type (Na-Cl-)	Ca	65% SO <sub>4</sub> – 24% Ca	52% SO <sub>4</sub> – 26% CO <sub>3</sub> – 19% Ca
Salts	Calcite-gyps.-ul.-hal.	Gyps.-hal.-mirab.-ul.	Gyps.-hal.-mirab.-ul.
Infiltration rate	~negligible	0.01-12.8% of outflow	0.01% - ~inflows

Thermal influence ( $T > 15^{\circ}\text{C}$ )	Yes	78 %	60%
Spring $T_{\text{max}}$	47 °C (20-75 °C*)	83 °C (Puchuldiza)	36 °C (Challviri)
Spring TDS (range)	14 g/l	3.8 g/l in average (0.2-21.8)	0.82 g/l in average (max. 14)
Mantle influence	47%	69%	44%
CO <sub>2</sub> isotopic composition	-11‰	-8 to -0.6‰	-20 to -6‰

596 Laguna Pastos Grandes is a calcic-type salar characterized by Na-Ca-Cl brines which can,  
597 according to thermodynamic models, lead to the precipitation of calcite, the first mineral  
598 of the evaporative pathway before gypsum and ulexite (Hardie and Eugster, 1970; Risacher  
599 and Fritz, 2009). Despite the fact that the calcic-type salar represents 19% of the salars in  
600 Bolivia (n=6) and 24% in Chile (n=12, Table 5), modern massive calcite precipitations are  
601 only observed in Laguna Pastos Grandes whereas gypsum, mirabilite (Na<sub>2</sub>SO<sub>4</sub>), halite and  
602 ulexite dominate other calcic salars. For example, Laguna Capina in Bolivia shows similar  
603 water chemistry and mineralogical characteristics to Laguna Pastos Grandes with the  
604 exception of its massive calcite precipitation (Ballivian and Risacher, 1981). This means  
605 that at least one other parameter than the Ca<sup>2+</sup> concentration varies between the Andean  
606 salars and controls the extent of calcite precipitation in Laguna Pastos Grandes. Despite  
607 the fact that carbonate mineral precipitation is tremendously complicated by  
608 biomineralization processes (mainly associated here with micro-organisms; Jones and  
609 Renaut, 1994) and reaction kinetics in a non-ideal near-surface continental environment  
610 (with ion interactions, variable substrates, fluctuating pH, organic molecules and gas phase  
611 interactions; Alonso-Zarza and Tanner, 2010), we can consider that the fundamental reason  
612 for calcite to precipitate in significant amounts is because both Ca<sup>2+</sup><sub>(aq)</sub> and CO<sub>3</sub><sup>2-</sup><sub>(aq)</sub> are  
613 supplied in sufficient concentrations by water inflows to dynamically sustain the  
614 supersaturation relative to calcite. The focus of our investigations is therefore on the origin  
615 of the CO<sub>2</sub> and Ca enrichments in water inflows.

## 616 **5.1 Origin of CO<sub>2</sub> and N<sub>2</sub> in thermal spring gases**

617 The thermal springs of Laguna Pastos Grandes discharge not only thermal waters but also  
618 gases that are essentially mixtures of CO<sub>2</sub> and N<sub>2</sub> (Table 1) like the other gas sources  
619 identified in the Central Andes (Spiro et al., 1997). Changes in the relative proportions of  
620 CO<sub>2</sub> and N<sub>2</sub> gas between sources in Laguna Pastos Grandes can be partly attributed to  
621 changes in the contribution from Air Saturated Waters (ASW) to the hydrothermal system  
622 feeding the carbonate platform. Indeed, the <sup>40</sup>Ar/<sup>36</sup>Ar mean value of 289.3 is close to the  
623 air value of 295.5 (Nier, 1950). The air-normalized abundances of the Atmosphere-Derived  
624 Noble Gases (ADNG: <sup>20</sup>Ne and <sup>36</sup>Ar) for all samples show a degree of depletion correlated  
625 with elemental mass of the noble gases (Ne > Ar), which is consistent with the water-  
626 solubility fractionation of air (Fig. 3). The atmospheric component found in thermal springs  
627 (including O<sub>2</sub> and the atmospheric proportion of N<sub>2</sub>) is therefore related to an ASW  
628 component and not the result of air-contamination during sampling.

629  
630 Despite this ASW component, the average R<sub>C</sub>/R<sub>A</sub> value of 3.79 ± 0.08 (Fig. 3, Table 1)  
631 indicates the presence of mantle-derived helium in the ascending hydrothermal flux. Our  
632 helium isotope results supplement and confirm previous data on the Central Andes  
633 including one isolated analysis in Laguna Pastos Grandes (Fig. A2; Hilton et al., 1993;  
634 Hoke et al., 1994). Assuming that pure mantle-derived helium is characterized by R<sub>C</sub>/R<sub>A</sub>  
635 ~8, we deduced that ~47 % of the helium at Laguna Pastos Grandes is of mantle origin  
636 (using calculations described in Hoke et al., 1994; Table 1) whereas it does not exceed 20%



637 in other gas sources from the Altiplano. In the Western Cordillera, however, the mantle  
638 helium contribution rises up to 69% at the Isluga volcano in Chile, 300 km north of Laguna  
639 Pastos Grandes close to the Chilean-Bolivian border (Hoke et al., 1994). Therefore, the  
640 particularly high mantle influence in Laguna Pastos Grandes compared with that of the  
641 Bolivian Altiplano is probably due to its proximity to the active volcanic arc of the Western  
642 Cordillera (Table 5; Springer and Förster, 1998). This is consistent with the fact that the  
643 Laguna Pastos Grandes' thermal springs also show the highest temperature recorded in  
644 salar springs in the Altiplano with a maximum temperature observed by Jones and Renaut  
645 (1994) of 75 °C and 46 °C in this study (Table 5). For comparison purposes, the maximum  
646 temperature recorded in the Western Cordillera is about 87 °C (Puchuldiza salar, northern  
647 Chile; Risacher et al., 2011).

648  
649 Yet, the average  $\delta^{13}\text{C}$  value of  $\text{CO}_2 \sim -11.1 \pm 0.1\text{‰}$  is lower than the typical value of a  
650 magmatic mantle-derived  $\text{CO}_2$  source (between -9 and -4‰; Hoefs, 1980). Two hypotheses  
651 can be proposed to explain this low value: a contribution of  $\text{CO}_2$  from sedimentary sources,  
652 i.e., organic carbon with  $\delta^{13}\text{C} < -20\text{‰}$  (Hoefs, 1980) or carbonate precipitation during fluid  
653 ascent. To trace the origin of the  $\text{CO}_2$ ,  $\delta^{13}\text{C}$  values of the gas samples are typically  
654 interpreted in relation to  $\text{CO}_2/{}^3\text{He}$  values (Sano and Marty, 1995). However, in Laguna  
655 Pastos Grandes, hydrothermal degassing and liquid-vapor partitioning could have  
656 significantly affected the  $\delta^{13}\text{C}$  and  $\text{CO}_2/{}^3\text{He}$  values of the gas. We thus determined the  
657  $\text{CO}_2/{}^3\text{He}$  composition at threshold P-T degassing conditions using calculations of fluid  
658 phase equilibria applied to our system ( $\text{H}_2\text{O}-\text{NaCl}-\text{CO}_2-\text{N}_2-\text{O}_2-\text{He}-\text{Ne}-\text{Ar}$ ; Rouchon et al.,  
659 2016). We assumed that all the gaseous  $\text{CO}_2$  had been exsolved at a single depth of  
660 supersaturation and that there were no carbonate precipitation effects on the  $\text{CO}_2/{}^3\text{He}$  value  
661 considering the acid pH  $\sim 6$  of hydrothermal fluids. The best results were obtained with an  
662 initial meteoric water recharge at high altitude, i.e., 5500 m, and with a temperature of 0  
663 °C. This is consistent with the  $\delta^{18}\text{O}$  and  $\delta^2\text{H}$  relationship in the spring waters, which  
664 suggests that the geothermal reservoir is fed during the wet season by meteoric water of  
665 rainfall isotopic composition (i.e.,  $\delta^{18}\text{O}$  of -16‰ and  $\delta^2\text{H}$  of -123‰; Fig. 4 and Table A2  
666 for values). Snow deposited during the dry season shows completely different isotopic  
667 compositions (minimum  $\delta^{18}\text{O}$  of -6.8‰ and  $\delta^2\text{H}$  of -30.3‰). Considering a local geotherm  
668 of 45 °C/km (Rothstein and Manning, 2003), we obtained between 17 and 49% of  $\text{CO}_2$   
669 exsolution at a degassing depth of approximately 25-35 m (at 2.5-3.5 bar) in the different  
670 springs (Table 1). Before degassing, the  $\text{CO}_2/{}^3\text{He}$  values were consequently higher than  
671 those measured at the surface and between  $4.7 \cdot 10^8$  and  $2.9 \cdot 10^9$ . These values are within  
672 the range or slightly lower than the mantle value of  $2 \cdot 10^9$  (Marty and Jambon, 1987). This  
673 depletion of  $\text{CO}_2$  relative to  ${}^3\text{He}$  in the fluids compared with the mantle value could be fully  
674 compatible with carbonate precipitation during the geothermal fluid ascent. Given that  
675 carbonates are enriched in  ${}^{13}\text{C}$  compared with  $\text{CO}_2$ , this would also explain why the  
676 remaining  $\text{CO}_2$  in the gas is depleted on  ${}^{13}\text{C}$ . We cannot, however, completely rule out a  
677 minor contribution from the organic matter of underlying but unknown sedimentary rocks  
678 possibly accompanied to some extent by carbonates, which could account for the small  
679 shift towards negative  $\delta^{13}\text{C}_{\text{CO}_2}$  values compared with the mantle.

680  
681 Likewise, the  $\delta^{15}\text{N}$  values between 2.3 and 6.4‰ could reflect a sedimentary ( $+10\text{‰} >$   
682  $\delta^{15}\text{N} > -5\text{‰}$ ; e.g. Ader et al. 2016) or crustal (mean  $\delta^{15}\text{N} = +7\text{‰}$ ; e.g. Sano et al., 1998)  
683 contribution mainly generated by organically sourced nitrogen sequestered in sedimentary  
684 rocks through biologic activity and sedimentation (Boyd, 2001). Although stratovolcanoes

685 and their products dominate the South Lipez landscape of the Altiplano (Avila-Salinas,  
686 1991; de Silva and Francis, 1991; Richter et al., 1992), the volcanic rocks have likely  
687 overlain (Ludington et al., 1975) or incorporated (Risacher and Alonso, 2001) Cretaceous  
688 and Early Tertiary clastic to evaporitic sediments. In particular, the Cretaceous El Molino  
689 Formation is known to contain several organic-rich units with TOC up to 4.2% (Camoin et  
690 al., 1991; Blanc-Valleron et al., 1994). Unfortunately, it remains unclear whether the El  
691 Molino Formation extends in the South Lipez region. Alternatively, this region being close  
692 to the subduction zone of the Nazca plate below the South American plate (with the slab  
693 located at a depth of ~150-km below the Altiplano; Hoke et al., 1994; Kay and Coira,  
694 2009), organic carbon and nitrogen may be remobilized from the slab by metamorphism  
695 (Gorman et al., 2006) and transported through primary melts into crustal intrusions. This  
696 hypothesis is supported by the high concentrations of Li associated with light  $\delta^7\text{Li}$  recorded  
697 in volcanic lava flows surrounding Laguna Pastos Grandes (compared with MORB  
698 composition representing the upper mantle,  $\delta^7\text{Li} = 3.7\text{‰}$  Misra et al., 2012), which can  
699 only be interpreted as the addition of highly-negative  $\delta^7\text{Li}$  slab-derived fluids component  
700 to the mantle wedge beneath our studied area (Fig. 8; Chan et al., 2002). Boron is also  
701 highly concentrated in the volcanic rocks of the area (30-144 ppm) and could derive from  
702 the same source as the Li. However,  $\delta^{11}\text{B}$  values, between -14 and -8‰ are more negative  
703 than the lowest value of the slab-derived fluids predicted for the Andes ( $> -2.8\text{‰}$ ; Rosner  
704 et al., 2003). B is more volatile than Li and light  $\delta^{11}\text{B}$  values are commonly observed in  
705 magmatic rocks (Chaussidon and Albarède, 1992) due to magma degassing effects, which  
706 produce  $^{11}\text{B}$  depletion in the residual melt (Jiang and Palmer, 1998).

707

708

## 5.2 Hydrological history of spring water

709

710 The question of the origin of spring waters in Andean salars has been examined in previous  
711 studies (Risacher and Fritz, 1991; Risacher et al., 2003; Risacher and Fritz, 2009). Risacher  
712 et al. (2003) proposed that saline lakes are continuously leaking through their bottom  
713 sediments, feeding most of the dissolved components to groundwater. In this case, the  
714 relative rate of infiltration and meteoric water recharge would control the lake's salinity  
715 and the concentration of conservative components in the system (Sanford and Wood,  
716 1991). We thus used the isotopic composition of the water to determine the origin (and the  
717 evolution) of the spring waters in Laguna Pastos Grandes. Spring waters lie on the local  
718 Ground and Spring Water Line (LGSWL) with slightly more positive  $\delta^{18}\text{O}$  and  $\delta^2\text{H}$  values  
719 than rainfall, implying evaporative enrichment in both  $^{18}\text{O}$  and  $^2\text{H}$  of the meteoric water  
720 prior to infiltration at high altitude (Fig. 4b; Bershaw et al., 2016). Another explanation for  
721 this enrichment could be the loss of vapor during the ascent of thermal fluids from the  
722 reservoir to the surface (Cortecci et al., 2005). The hydrothermal springs are thus  
723 genetically linked to the meteoric waters. The Piedmont thermal source, which is the  
724 coldest spring (32 °C), less saline than others, and located on the border of the laguna,  
725 shows more negative  $\delta^{18}\text{O}$  and  $\delta^2\text{H}$  values, suggesting a dilution of thermal spring water  
726 by meteoric water (Fig. 4). By comparison, the brine of the laguna is very enriched in  $^{18}\text{O}$   
727 and  $^2\text{H}$ , ruling out the hypothesis of an important recharge of the springs by infiltration of  
728 the laguna brine. The Cl/Br values of spring waters are also not consistent with a dilution  
729 of recycled brines by mixing with groundwater or meteoric water (Fig. 5c). It suggests that  
730 the chemistry of the spring waters more likely derives from the alteration of the bedrock  
731 minerals.

### 5.3 Volcanic bedrock alteration at high temperature and pCO<sub>2</sub>

$\delta^7\text{Li}$  and Na/K geothermometers applied to spring waters indicate that the meteoric water reached a maximum temperature of 200-250 °C after infiltration. Due to the high mantle-derived CO<sub>2</sub> flux delivered in thermal springs, the estimated pCO<sub>2</sub> in these waters (between 3 and 389 mbar estimated by PHREEQC; Table 2) spans the range and even exceeds the pCO<sub>2</sub> in spring waters from both the Altiplano and the Western Cordillera with 40 – 120, and 10 – 340 mbar, respectively (Morteani et al., 2014). This CO<sub>2</sub> enrichment can acidify thermal waters to a pH ~5 and give groundwater the ability to dissolve the bedrock minerals and acquire a large enrichment in solute load and especially in Ca. To test this hypothesis, we performed a series of PHREEQC modeling to determine the water composition resulting from the alteration of the volcanic bedrock with possible evaporites (halite, gypsum and anhydrite) from a meteoric water at 200, 225 and 250 °C with different CO<sub>2</sub> partial pressures and compared the results with the average spring water composition (Table A4; Fig. 7).

The best results for Ca, Mg and K concentrations in spring waters were obtained by the alteration of volcanic minerals at a temperature of 225 °C, which is the average temperature determined using geothermometers, and 20 bar of CO<sub>2</sub> (Fig. 7). This amount of CO<sub>2</sub> is compatible with the proximity of an ancient pre-eruptive magma reservoir of the volcano at a depth of ~3 km as suggested by de Silva and Kay (2018). Under these conditions, the main source of Ca in the water is the dissolution of Ca-rich feldspars rather than anhydrite (Table A4). These results are corroborated by Sr isotope data, which suggest that local meteoric waters interact with the host volcanic rocks (dacite, andesite and rhyolitic ignimbrite) rather than with ancient marine carbonates (Fig. 6a). Similarly, thermal waters and the laguna brine show  $\delta^7\text{Li}$  and  $\delta^{11}\text{B}$  values not far from those of the surrounding volcanic rocks (Fig. 6b).  $\delta^7\text{Li}$  values measured in waters are on average 8‰ higher than those measured in the surrounding rocks. This shift has been commonly observed in hydrothermal systems (e.g., von Strandmann et al., 2006; Godfrey et al., 2013) and experimental works showed that the difference between the  $\delta^7\text{Li}$  values of the water and weathered volcanic rocks must be due to equilibrium isotopic fractionation at high temperature ( $\Delta^7\text{Li}$  between 9.5‰ at 200 °C and 6.7‰ at 250 °C; Millot et al., 2010). The average 7‰ positive  $\delta^{11}\text{B}$  shift between springs and volcanic rocks can be explained either by adsorption of B on mineral surfaces during the ascent and cooling of hydrothermal fluid to the spring vent or by the preferential incorporation of light B during carbonate precipitation.

The water chemistry obtained with these simulations is over-saturated with different carbonate minerals ( $\text{SI}_{\text{calcite}}=1.23$ ,  $\text{SI}_{\text{dolomite}}=3.03$ ,  $\text{SI}_{\text{magnesite}}=2.02$ ), which supports the hypothesis deduced from CO<sub>2</sub>/<sup>3</sup>He and  $\delta^{13}\text{C}$  data that carbonate could have precipitated during fluid ascent. The higher Si concentration obtained in our simulations compared with those measured in spring waters together with the low temperature given by the SiO<sub>2</sub> geothermometer also indicate precipitation of silica during fluid ascent. The simulations suggest, however, that the salinity of the spring water is most probably delivered by the dissolution of halite deposits. This interpretation is confirmed by the homogeneous  $\delta^{37}\text{Cl}$  values of the springs of  $0.25\pm 0.03\%$  on average (n=12; Table A3), which are close to the  $\delta^{37}\text{Cl}$  value expected for the precipitation of halite in equilibrium with seawater at 0‰ and 25 °C ( $\delta^{37}\text{Cl} = 0.30\%$ ; Eggenkamp et al., 1995, 2016). It indicates that over time, multiple cycles of precipitation and dissolution of halite without new inputs of Cl to the laguna have

780 homogenized the Cl isotopic composition of the laguna brine and salts. Therefore, we can  
781 assume that Na and Cl derive from ancient marine halite deposits, which could have formed  
782 during the last Cenomanian-Turonian marine period. In the studied area, these deposits,  
783 which have been remobilized in the continental overlying Cretaceous and Tertiary deposits  
784 (Deconinck et al., 2000), could have been either overlain by volcanic rocks or incorporated  
785 by volcanic eruptions as suggested by Risacher and Alonso (2001) for gypsum. This is also  
786 consistent with Cl and Na concentrations in these waters, which display a covariant trend  
787 close to equimolarity, typical of halite leaching (Fig. A3).

788

#### 789 **5.4 How is Laguna Pastos Grandes unique?**

790

791 Ca:alkalinity molar ratios of the different waters of Laguna Pastos Grandes show that only  
792 the thermal springs have the potential to precipitate calcite (Fig. 5b). Stream waters and  
793 mixed sources (Piedmont) are too diluted to contribute to the growth of the carbonate  
794 platform, and the laguna brine, which derives from the spring waters (as suggested by Sr,  
795 chemical and isotopic data; Figs. 4, 5, 6) has been depleted in carbonate relative to Ca.  
796 Most of the salars in the Central Andes are fed by thermal spring inflows (60% in Bolivia  
797 and 78% in Chile) enriched in solutes compared with streams and regional groundwater  
798 (Table 5; Risacher and Fritz, 1991; Risacher et al., 2011). However, modern carbonate is  
799 absent or minor in these systems and generally precipitated as the first mineral of a more  
800 developed evaporitic sequence (Risacher and Fritz, 2009). Laguna Pastos Grandes is  
801 unique in this respect, as it displays a ~40 km<sup>2</sup> recent-to-modern carbonate platform  
802 spatially associated with thermal waters. These waters not only show a remarkable mantle  
803 influence on temperature and gas composition but also one of the highest enrichments in  
804 solutes of the Central Andes with an average salinity of 14 g/l (Fig. 8; Table 5). This could  
805 be indicative of the significant alteration rate of the hydrothermal system of Laguna Pastos  
806 Grandes compared with the other salars due to the high flow of CO<sub>2</sub> gas from the mantle.  
807 Moreover, the singularity of this laguna is also likely related to a particular mineralogy of  
808 the volcanic bedrock since calcic-type salars are limited in the Andean region. For example,  
809 Chilean volcanic rocks are known to be particularly enriched in sulfides (Risacher and  
810 Alonso, 2001) and could be responsible for the genesis of a majority of sulfate-type salars  
811 (65%) rather than calcic-type salars.

#### 812 **6. Conclusion and perspectives**

813 To the first order, Bolivian and Chilean salars belong to the same climatic, geologic and  
814 hydrologic environment (Risacher and Fritz, 2009). Nevertheless, they present a great  
815 diversity of chemistry and salt types, which result from local variations in fluid sources and  
816 climate parameters. We have shown in this study that the western part of Laguna Pastos  
817 Grandes, characterized by abundant recent-to-modern carbonate deposits, is mainly fed by  
818 thermal spring water with minor contributions of rainfall and surrounding streams, all of  
819 meteoric origin. These spring waters show Ca<sup>2+</sup><sub>(aq)</sub> and CO<sub>3</sub><sup>2-</sup> in sufficient concentrations  
820 to be over-saturated with calcite. Both solutes can originate from the alteration of the  
821 volcanic bedrock by highly CO<sub>2</sub>-enriched fluids heated at ~225 °C. The magmatic mantle-  
822 derived CO<sub>2</sub> and the particularly high heat flow that drive the fluid circulation to the surface  
823 are probably due to a shallow pre-eruptive magma chamber as suggested by de Silva et al.  
824 (2006) and de Silva and Kay (2018) (i.e., at a typical depth of ~5 km; Fig. 8). This  
825 configuration thus fulfills all the essential criteria to provide solutes and precipitate large  
826 volumes of carbonates in comparison with most other modern Andean salars.

827  
828 This configuration is not exclusive to the Andean geodynamic system and can be found in  
829 many continental extensional settings (e.g., in Afar) where we posit, by analogy, that the  
830 same mechanisms act as key factors in the genesis of continental carbonate deposits in pure  
831 volcanic provinces. The main components of this favorable configuration would be, as  
832 identified in this study, a deep source of CO<sub>2</sub> and the Ca-rich volcanic basement allowing  
833 the following processes to occur:

834 i. Alteration of a sulfide-poor volcanic bedrock containing Ca-enriched minerals  
835 (usually feldspars) at high pCO<sub>2</sub> and high temperature, leading to cationic enrichment of  
836 the waters and producing calcic type hydrothermal waters.

837 ii. When the hydrothermal waters emerge at the surface as springs and encounter  
838 the much lower atmospheric levels of pCO<sub>2</sub>, CO<sub>2</sub> is massively degassed leading to a pH  
839 increase. These concomitant processes drive the solution to precipitate carbonates. CO<sub>2</sub>  
840 loss may also be driven by photosynthesis.

841 iii. High evaporation rates at the surface, increasing the solute concentrations above  
842 calcite saturation.

843  
844 Laguna Pastos Grandes is, therefore, a unique natural laboratory that shows a great  
845 diversity of carbonate facies (including pisoliths, ooids, muds and microbialites; Risacher  
846 and Eugster, 1979; Jones and Renault, 1994; Bougeault et al., 2019), some of them  
847 remarkably similar to ancient equivalents such as Cretaceous Presalt carbonates (Terra et  
848 al., 2010; Tosca and Wright, 2015; Muniz and Bosence, 2015). This laguna could,  
849 therefore, be further used to trace the biotic and/or abiotic controls at play in the formation  
850 of these carbonate deposits. Indeed, microbial mats and thin, dark, mucilaginous films  
851 locally coating the pool floors and pisolith surfaces in Laguna Pastos Grandes (described  
852 by Jones and Renault, 1994 and Bougeault et al., 2019) might also contribute to the  
853 carbonate precipitation (Pace et al., 2018; Gomez et al., 2018). Comprehensive  
854 geochemical, mineralogical and biodiversity studies are underway on the whole carbonate  
855 platform of Pastos Grandes to characterize the link between physicochemical parameters,  
856 microbial communities and the diversity of carbonate fabrics observed. These results will  
857 provide clues to identify the biosignatures in modern microbialites and enable us to further  
858 interpret the sedimentary record on our planet and beyond.

## 859 **Acknowledgments, Samples, and Data**

860 We would like to thank Total E&P Bolivia for field assistance (Serge Nicoletis, Jean-Pierre  
861 Meunier, Olivier-Daniel Moreau, Rozmarie Cuellar) and Total Lab (CSTJF, Pau, France;  
862 Carole Bortelle, Josiane Sentenac, Valérie Burg) for water analysis; Mathilde Mercuzot  
863 (Univ. Burgundy) for field and laboratory assistance (2016); Antoine Coge for strontium  
864 isotopic analysis of volcanic rocks, Pierre Burckel for the chemical composition analysis  
865 of volcanic rocks, and BRGM (Catherine Guerrot team) for the chemical and isotopic  
866 measurements in water samples (2016). We would also like to thank Dr. Daniel Carrizo for  
867 providing the Chilean geological map. Particular thanks go to Magali Bonifacie for the  
868 constructive discussion on chlorine isotope data. Funding was provided by Total EP R&D  
869 Carbonate Project (E. Poli). Parts of this work were supported by IPGP's multidisciplinary  
870 program PARI, and by the Paris-IdF region SESAME Grant no. 12015908.  
871 This is IPGP contribution No. 4062.

872 **References**

- 873 Ader M., Thomazo C., Sansjofre P., Busigny V., Papineau D., Laffont R., ... and  
874 Halverson G. P. (2016) Interpretation of the nitrogen isotopic composition of  
875 Precambrian sedimentary rocks: Assumptions and perspectives. *Chemical Geology* **429**,  
876 93-110.
- 877 Ahlfeld F. (1956) Sodaseen in Lipez (Bolivien). *Neues Jb. Miner. Mh.* **6/7**, 128-136.
- 878 Ahlfeld F. and Branisa L. (1960) Geologia de Bolivia: Instituto Boliviano del Petróleo,  
879 Ed. Dom  
880 Bosco, La Paz.
- 881 Alonso-Zarza A. M. and Tanner L. H. (2010) Carbonates in continental settings: Facies,  
882 environments, and processes: Developments in Sedimentology **61**, pp. 378.
- 883 Assayag N., Jézéquel D., Ader M., Viollier E., Michard G., Prévot F., and Agrinier P.  
884 (2008) Hydrological budget, carbon sources and biogeochemical processes in Lac Pavin  
885 (France): constraints from  $\delta^{18}\text{O}$  of water and  $\delta^{13}\text{C}$  of dissolved inorganic carbon. *Applied*  
886 *Geochemistry* **23**(10), 2800-2816.
- 887 Avila-Salinas S. (1991) Petrologic and tectonic evolution of the Cenozoic volcanism in  
888 the Bolivian western Andes. In *Andean Magmatism And Its Tectonic Setting* (eds. R.S.  
889 Harmon and C.W. Rapela). Spec. Pap. geol. Soc. Am. **265**, 245-257.
- 890 Ballivian O. and Risacher F. (1981) Los salares del altiplano boliviano: métodos de  
891 estudio y estimación económica. IRD Editions.
- 892 Bershaw J., Saylor J.E., Garziona C.N., Leier A. and Sundell K.E. (2016) Stable isotope  
893 variations ( $\delta^{18}\text{O}$  and  $\delta^2\text{H}$ ) in modern waters across the Andean Plateau. *Geochimica et*  
894 *Cosmochimica Acta* **194**, 310–324.
- 895 Blanc P., Lassin A., Piantone P., Azaroual M., Jacquemet N., Fabbri A., and Gaucher  
896 E.C. (2012) Thermoddem: A geochemical database focused on low temperature  
897 water/rock interactions and waste materials. *Applied Geochemistry* **27**(10), 2107-2116.
- 898 Blanc-Valleron M.-M., Schuler M., Rauscher R., Camoin G. and Rouchy J.-M. (1994) La  
899 matière organique des séries d'âge Crétacé supérieur-Tertiaire inférieur du bassin de  
900 Potosi (Cordillère orientale, Bolivie): apports stratigraphiques et paléo-géographiques.  
901 *C.R. Acad. Sci. Paris II* **319**, 1359-1366.
- 902 Bonifacie M., Charlou J. L., Jendrzewski N., Agrinier P. and Donval J. P. (2005)  
903 Chlorine isotopic compositions of high temperature hydrothermal vent fluids over ridge  
904 axes. *Chemical Geology* **221**(3-4), 279-288.
- 905 Boschetti T., Cortecchi G., Barbieri M. and Mussi M. (2007) New and past geochemical  
906 data on fresh to brine waters of the Salar de Atacama and Andean Altiplano, northern  
907 Chile. *Geofluids* **7**(1), 33-50.
- 908 Boschetti T., Toscani L., Iacumin P. and Selmo E. (2017) Oxygen, Hydrogen, Boron and  
909 Lithium Isotope Data of a Natural Spring Water with an Extreme Composition: A Fluid  
910 from the Dehydrating Slab? *Aquatic Geochemistry* **23**(5-6), 299-313.
- 911 Boyd, S. R. (2001). Nitrogen in future biosphere studies. *Chemical Geology* **176**(1-4), 1-  
912 30.
- 913 Camoin G., Rouchy J.M., Babinot J.F. Deconinck J.F. and Tronchetti G. (1991)  
914 Dynamique sédimentaire et évolution paléogéographique d'un bassin continental en  
915 position d'arrière-arc: le Maastrichtien de la Cordillère orientale (Bolivie). *C.R. Acad.*  
916 *Sci. Paris II* **312**, 1335-1341.
- 917 Chaffaut I., Coudrain-Ribstein A., Michelot J. L. and Pouyaud B. (1998) Précipitations  
918 d'altitude du Nord-Chili, origine des sources de vapeur et données isotopiques. *Bull. Inst.*  
919 *Fr. Etudes andines* **27**, 367-384 (in French).

920 Chan L.H., Edmond J.M., Thompson G. and Gillis K. (1992) Lithium isotopic  
921 composition of submarine basalts: implications for the lithium cycle in the oceans. *Earth*  
922 *Planet. Sci. Lett.* **108**, 151–160.

923 Chan L.H. and Kastner, M. (2000) Lithium isotopic composition of pore fluids and  
924 sediments in the Costa Rica subduction zone: implications for fluid processes and  
925 sediment contribution to arc volcanoes. *Earth Planet. Sci. Lett.* **183**, 275–290.

926 Chan L. H., Leeman W. P. and You C. F. (2002) Lithium isotopic composition of Central  
927 American volcanic arc lavas: implications for modification of subarc mantle by slab-  
928 derived fluids: correction. *Chemical Geology* **182**(2-4), 293-300.

929 Chaussidon M. and Marty B. (1995) Primitive boron isotope composition of the mantle.  
930 *Science* **269**, 383–386.

931 Chetelat B., Liu C.-Q., Gaillardet J., Wang Q.L., Zhao Z.Q., Liang C.S., Xiao Y.K.  
932 (2009) Boron isotopes geochemistry of the Changjiang basin rivers. *Geochim.*  
933 *Cosmochim. Acta* **73**, 6084-6097.

934 Claypool G. E., Holser W. T., Kaplan I. R., Sakai H. and Zak I. (1980) The age curves of  
935 sulfur and oxygen isotopes in marine sulfate and their mutual interpretation. *Chemical*  
936 *Geology* **28**, 199-260.

937 Cortecchi G., Boschetti T., Mussi M., Lameli C. H., Mucchino C. and Barbieri M. (2005)  
938 New chemical and original isotopic data on waters from El Tatio geothermal field,  
939 northern Chile. *Geochemical Journal* **39**(6), 547-571.

940 Deconinck J. F., Blanc-Valleron M. M., Rouchy J. M., Camoin G. and Badaut-Trauth D.  
941 (2000) Palaeoenvironmental and diagenetic control of the mineralogy of Upper  
942 Cretaceous–Lower Tertiary deposits of the Central Palaeo–Andean basin of Bolivia  
943 (Potosi area). *Sedimentary Geology* **132**(3-4), 263-278.

944 Dellinger M., Gaillardet J., Bouchez J., Calmels D., Louvat P., Dosseto A., Gorge C.,  
945 Alanoca L. and Maurice L. (2015) Riverine Li isotope fractionation in the Amazon River  
946 basin controlled by the weathering regimes. *Geochimica et Cosmochimica Acta* **164**, 71-  
947 93.

948 de Silva S. L. and Francis P. W. (1991) *Volcanoes of the Central Andes*. Springer Verlag,  
949 Berlin.

950 de Silva S., Zandt G., Trumbull R., Viramonte J. G., Salas G. and Jimenez N. (2006)  
951 Large ignimbrite eruptions and volcano-tectonic depressions in the Central Andes: a  
952 thermomechanical perspective. In: Trois, C., De Natale, G., Kilburn, C.R.J. (Eds.),  
953 *Mechanism of Activity and Unrest at Large Calderas*, vol. 269. Geol. Soc. London, Spec.  
954 Publ., pp. 47-63.

955 de Silva S. and Kay S.M. (2018) Turning up the Heat: High-Flux Magmatism in the  
956 Central Andes. *Elements* **14**, 245-250.

957 Durand N., Monger H. C., Cinti M. G. and Verrecchia E. P. (2018) Calcium carbonate  
958 features. In *Interpretation of micromorphological features of soils and regoliths*. Elsevier.  
959 pp. 205-258.

960 Eggenkamp H. (1994)  $\delta^{37}\text{Cl}$ : The geochemistry of chlorine isotopes. Faculteit  
961 Aardwetenschappen, Universiteit Utrecht. *Geologica Ultraiectina*, (116).

962 Eggenkamp H.G.M., Kreulen R., and Koster Van Groos A.F., (1995) Chlorine stable  
963 isotope fractionation in evaporites. *Geochim. Cosmochim. Acta* **59** (24), 5169–5175.

964 Eggenkamp H. G. M., Bonifacie M., Ader M., and Agrinier P. (2016) Experimental  
965 determination of stable chlorine and bromine isotope fractionation during precipitation of  
966 salt from a saturated solution. *Chemical Geology* **433**, 46-56.

967 Flesch G. D., Anderson Jr A. R. and Svec H. J. (1973) A secondary isotopic standard for  
968  $^6\text{Li}/^7\text{Li}$  determinations. *International Journal of Mass Spectrometry and Ion Physics*  
969 **12**(3), 265-272.

970 Fouillac C. and Michard G. (1981) Sodium/lithium ratio in water applied to  
971 geothermometry of geothermal reservoirs. *Geothermics* **10**(1), 55-70.

972 Fournier R. O. and Potter Ii R. W. (1979) Magnesium correction to the Na/K/Ca chemical  
973 geothermometer. *Geochimica et Cosmochimica Acta* **43**(9), 1543-1550.

974 Fritz P., Suzuki O., Silva C. and Salati E. (1981) Isotope hydrology of groundwaters in  
975 the Pampa Del Tamarugal, Chile. *Journal of Hydrology* **53**, 161-184.

976 Gaillardet J. and Allègre C. J. (1995) Boron isotopic compositions of corals: Seawater or  
977 diagenesis record? *Earth and Planetary Science Letters* **136**(3-4), 665-676.

978 Giunta T., Ader M., Bonifacie M., Agrinier P. and Coleman M. (2015a) Pre-  
979 concentration of chloride in dilute water-samples for precise  $\delta^{37}\text{Cl}$  determination using a  
980 strong ion-exchange resin: Application to rainwaters. *Chemical Geology* **413**, 86-93.

981 Godfrey L. V., Chan L. H., Alonso R. N., Lowenstein T. K., McDonough W. F., Houston  
982 J., Li J., Bobst A. and Jordan T. E. (2013) The role of climate in the accumulation of  
983 lithium-rich brine in the Central Andes. *Applied Geochemistry* **38**, 92-102.

984 Godon A., Jendrzewski N., Eggenkamp H. G., Banks D. A., Ader M., Coleman M. L.  
985 and Pineau F. (2004) A cross-calibration of chlorine isotopic measurements and  
986 suitability of seawater as the international reference material. *Chemical Geology* **207**(1-  
987 2), 1-12.

988 Gomez F. J., Kah L. C., Bartley J. K. and Astini R. A. (2014) Microbialites in a high-  
989 altitude Andean lake: multiple controls on carbonate precipitation and lamina accretion.  
990 *Palaios* **29**(6), 233-249.

991 Gomez F. J., Mlewski C., Boidi F. J., Farías M. E. and Gérard E. (2018) Calcium  
992 carbonate precipitation in diatom-rich microbial mats: the Laguna Negra hypersaline  
993 lake, Catamarca, Argentina. *Journal of Sedimentary Research* **88**(6), 727-742.

994 Gorman P. J., Kerrick D. M. and Connolly J. A. D. (2006) Modeling open system  
995 metamorphic decarbonation of subducting slabs. *Geochemistry, Geophysics, Geosystems*  
996 **7**(4).

997 Hardie L. A. and Eugster H. P. (1970) The evolution of closed-basin brines.  
998 *Mineralogical Society of America Special Paper* **3**, 273-290.

999 Hilton D. R., Hammerschmidt K., Teufel S. and Friedrichsen H. (1993) Helium isotope  
1000 characteristics of Andean geothermal fluids and lavas. *Earth and Planetary Science*  
1001 *Letters* **120**(3-4), 265-282.

1002 Hoefs J. (1980) *Stable isotope geochemistry*. Berlin and Heidelberg, Springer Verlag.

1003 Hoke L., Hilton D. R., Lamb S. H., Hammerschmidt K. and Friedrichsen H. (1994)  $^3\text{He}$   
1004 evidence for a wide zone of active mantle melting beneath the Central Andes. *Earth and*  
1005 *Planetary Science Letters* **128**(3-4), 341-355.

1006 Horita J. (2014) Oxygen and carbon isotope fractionation in the system dolomite–water–  
1007  $\text{CO}_2$  to elevated temperatures. *Geochimica et Cosmochimica Acta* **129**, 111-124.

1008 Hurlbert S. H. and Chang C. C. (1984) Ancient ice islands in salt lakes of the Central  
1009 Andes. *Science* **224**(4646), 299-302.

1010 Iltis A., Risacher F. and Servant-Vildary S. (1984) Contribution à l'étude hydrobiologique  
1011 des lacs salés du sud de l'Altiplano bolivien. *Revue d'Hydrobiologie Tropicale* **17**(3),  
1012 259-273.

1013 Javoy M., Pineau F. and Delorme H. (1986) Carbon and nitrogen isotopes in the mantle.  
1014 *Chemical Geology* **57**(1-2), 41-62.



1015 Jones B. and Renaut R. W. (1994) Crystal fabrics and microbiota in large pisoliths from  
1016 Laguna Pastos Grandes, Bolivia. *Sedimentology* **41**(6), 1171-1202.

1017 Kaiser J. F. (2014) Understanding large resurgent calderas and associated magma  
1018 systems: the Pastos Grandes Caldera Complex, southwest Bolivia. PhD thesis of Oregon  
1019 State University.

1020 Kaiser J. F., de Silva S., Schmitt A. K. Economos R. and Sunagua M. (2017) Million-  
1021 year melt–presence in monotonous intermediate magma for a volcanic–plutonic  
1022 assemblage in the Central Andes: contrasting histories of crystal-rich and crystal-poor  
1023 super-sized silicic magmas. *Earth and Planetary Science Letters* **457**, 73-86.

1024 Kay S. M. and Coira B. L. (2009) Shallowing and steepening subduction zones,  
1025 continental lithospheric loss, magmatism, and crustal flow under the Central Andean  
1026 Altiplano-Puna Plateau. Backbone of the Americas: shallow subduction, plateau uplift,  
1027 and ridge and terrane collision, 204, 229.

1028 Kharaka Y. K., Lico M. S. and Law L. M. (1982) Chemical geothermometers applied to  
1029 formation waters, Gulf of Mexico and California basins. *AAPG Bulletin* **66**(5), 588-588.

1030 Kharaka Y. K. and Mariner R. H. (1989) Chemical geothermometers and their  
1031 application to formation waters from sedimentary basins. In *Thermal history of*  
1032 *sedimentary basins*. Springer, New York, NY. pp. 99-117.

1033 Kussmaul S., Hörmann P. K., Ploskonka E. and Subieta T. (1977) Volcanism and  
1034 structure of southwestern Bolivia. *Journal of Volcanology and Geothermal Research*  
1035 **2**(1), 73-111.

1036 Lemarchand D., Gaillardet J., Göpel C., Manhès G. (2002) An optimized procedure for  
1037 boron separation and mass spectrometry analysis for river samples. *Chemical Geology*  
1038 **182**, 323-334.

1039 Li L., Cartigny P. and Ader M. (2009) Kinetic nitrogen isotope fractionation associated  
1040 with thermal decomposition of NH<sub>3</sub>: Experimental results and potential applications to  
1041 trace the origin of N<sub>2</sub> in natural gas and hydrothermal systems. *Geochimica et*  
1042 *Cosmochimica Acta* **73**(20), 6282-6297.

1043 Louvat P., Moureau J., Paris G., Bouchez J., Noireaux J., Gaillardet J. (2014) A fully  
1044 automated direct injection nebulizer (d-DIHEN) for MC-ICP-MS isotope analysis:  
1045 application to boron isotope ratio measurements. *Journal of Analytical Atomic*  
1046 *Spectrometry* **29**(9), 1698-1707.

1047 Lowenstern J. B. (2001) Carbon dioxide in magmas and implications for hydrothermal  
1048 systems. *Mineralium Deposita* **36**(6), 490-502.

1049 Ludington S., Orris G.J., Cox D.P., Long K.R. and Asher-Bolinden S. (1975) Mineral  
1050 deposit models. In *Geology and Mineral Resources of the Altiplano and the Cordillera*  
1051 *Occidental, Bolivia* (eds Bleiwas D. J. and Christiansen R. G.). U.S. Geol. Survey Bull.  
1052 pp. 63-224.

1053 Ludington S., Orris G.J., Cox D.P., Long K.R. and Asher-Bolinder S. (1992) Mineral  
1054 deposit models. In *Geology And Mineral Resources Of The Altiplano and Cordillera*  
1055 *Occidental, Bolivia* (eds by U.S. Geological Survey and Servicio Geolbgico de Bolivia).  
1056 Bull. US geol. Surv. 1975, pp. 63-89.

1057 Marty B. and Jambon A. (1987) <sup>3</sup>He in volatile fluxes from the solid Earth: Implications  
1058 for carbon geodynamics. *Earth Planetary Science Letter* **83**, 16-26.

1059 McArthur J. M., Kennedy W. J., Chen M., Thirlwall M. F. and Gale A. S. (1994)  
1060 Strontium isotope stratigraphy for Late Cretaceous time: direct numerical calibration of  
1061 the Sr isotope curve based on the US Western Interior. *Palaeogeography,*  
1062 *Palaeoclimatology, Palaeoecology* **108**(1-2), 95-119.

1063 Millot R., Guerrot C. and Vigier N. (2004) Accurate and high-precision measurement of  
1064 lithium isotopes in two reference materials by MC-ICP-MS. *Geostandards and*  
1065 *Geoanalytical Research* **28**(1), 153-159.

1066 Millot R., Scaillet B. and Sanjuan B. (2010) Lithium isotopes in island arc geothermal  
1067 systems: Guadeloupe, Martinique (French West Indies) and experimental approach.  
1068 *Geochimica et Cosmochimica Acta* **74**, 1852-1871.

1069 Moquet J. S., Crave A., Viers J., Seyler P., Armijos E., Bourrel L., Chavarri E.N, Lagane  
1070 C., Laraque A., Lavado Casimiro W.S., Pombosa R., Noriega L., Vera A. and Guyot J.L.  
1071 (2011) Chemical weathering and atmospheric/soil CO<sub>2</sub> uptake in the Andean and  
1072 Foreland Amazon basins. *Chemical Geology* **287**(1-2), 1-26.

1073 Moreira M., Rouchon V., Muller E. and Noirez S. (2018) The xenon isotopic signature of  
1074 the mantle beneath Massif Central. *Geochemical Perspectives Letters* **6**, 28-32.

1075 Moriguti, T., and Nakamura, E. (1998) Across-arc variation of Li isotopes in lavas and  
1076 implications for crust/mantle recycling at subduction zones. *Earth and planetary science*  
1077 *letters* **163**(1-4), 167-174.

1078 Morris R.V., Ruff S.W., Gellert R., Ming D.W., Arvidson R.E., Clark B.C., Golden C.C.,  
1079 Siebach K., Klingelhöfer G., Schröder C., Fleischer I., Yen A.S. and Squyres W. (2010)  
1080 Identification of carbonate-rich outcrops on Mars by the Spirit rover. *Science* **1189667**.

1081 Morteani G., Möller P., Dulski P. and Preinfalk C. (2014) Major, trace element and stable  
1082 isotope composition of water and muds precipitated from the hot springs of Bolivia: Are  
1083 the waters of the spring's potential ore forming fluids? *Chemie der Erde-Geochemistry*  
1084 **74**(1), 49-62.

1085 Nier A. O. (1950) A redetermination of the relative abundances of the isotopes of carbon,  
1086 nitrogen, oxygen, argon and potassium. *Physical Review* **77**(6), 789-793.

1087 Ozima M. and Podosek F. A. (2002) *Noble Gas Geochemistry*. Cambridge University  
1088 Press.

1089 Pace A., Bourillot R., Bouton A., Vennin E., Braissant O., Dupraz C., Duteil T.,  
1090 Bundeleva I., Patrier P., Galaup S., Yokoyama Y., Franceschi M., Virgone A. and  
1091 Visscher P.T. (2018) Formation of stromatolite lamina at the interface of oxygenic–  
1092 anoxygenic photosynthesis. *Geobiology* **16**(4), 378-398.

1093 Parkhurst D.L. and Appelo C.A.J. (2013) Description of input and examples for  
1094 PHREEQC version 3 – a computer program for speciation, batch-reaction, one-  
1095 dimensional transport, and inverse geochemical calculations. U.S. geological survey  
1096 techniques and methods, book 6, chap. A43, pp 497.

1097 Pierret M. C., Clauer N., Bosch D., Blanc G. and France-Lanord C. (2001). Chemical and  
1098 isotopic (<sup>87</sup>Sr/<sup>86</sup>Sr, δ<sup>18</sup>O, δD) constraints to the formation processes of Red-Sea brines.  
1099 *Geochimica et Cosmochimica Acta* **65**(8), 1259-1275.

1100 Pin C. and Bassin C. (1992) Evaluation of a strontium-specific extraction  
1101 chromatographic method for isotopic analysis in geological materials. *Analytica Chimica*  
1102 *Acta* **269**(2), 249-255.

1103 Pineau F. and Javoy M. (1983) Carbon isotopes and concentrations in mid-Atlantic ridge  
1104 basalts. *Earth Planetary Science Letter* **29**, 413-421.

1105 Pistiner J.S. and Henderson G.M. (2003) Lithium-isotope fractionation during continental  
1106 weathering processes. *Earth Planetary Science Letter* **214** (1–2), 327-339.

1107 von Strandmann, P. A. P., Burton, K. W., James, R. H., van Calsteren, P., Gíslason, S. R.,  
1108 and Mokadem, F. (2006). Riverine behaviour of uranium and lithium isotopes in an  
1109 actively glaciated basaltic terrain. *Earth and Planetary Science Letters* **251**(1-2), 134-  
1110 147.

1111 Richter D. H., Luddington S. and Soria-Escalante E. (1992) Geologic setting. In Geology  
1112 and mineral resources of the Altiplano and Cordillera Occidental, Bolivia (eds by U.S.  
1113 Geological Survey and Servicio Geolbgico de Bolivia), US. geol. Surv. Bull., 1975, 14-  
1114 24.

1115 Risacher F. (1978) Le cadre géochimique des bassins à évaporites des Andes boliviennes.  
1116 Cahiers ORSTOM. *Série Géologie* **10**(1), 37-48.

1117 Risacher F. and Eugster H. P. (1979) Holocene pisoliths and encrustations associated  
1118 with spring-fed surface pools, Pastos Grandes, Bolivia. *Sedimentology* **26**(2), 253-270.

1119 Risacher F. and Fritz B. (1991) Geochemistry of Bolivian salars, Lipez, southern  
1120 Altiplano: origin of solutes and brine evolution. *Geochimica et Cosmochimica Acta*  
1121 **55**(3), 687-705.

1122 Risacher F., and Alonso H. (2001) Geochemistry of ash leachates from the 1993 Lascar  
1123 eruption, northern Chile. Implication for recycling of ancient evaporites. *Journal of*  
1124 *volcanology and geothermal research* **109**(4), 319-337.

1125 Risacher F. and Fritz B. (2009) Origin of salts and brine evolution of Bolivian and  
1126 Chilean salars. *Aquatic Geochemistry* **15**(1-2), 123-157.

1127 Risacher F., Alonso H. and Salazar C. (2003) The origin of brines and salts in Chilean  
1128 salars: a hydrochemical review. *Earth-Science Reviews* **63**(3-4), 249-293.

1129 Risacher F., Fritz B. and Hauser A. (2011) Origin of components in Chilean thermal  
1130 waters. *Journal of South American Earth Sciences* **31**(1), 153-170.

1131 Rissmann C., Leybourne M., Benn C. and Christenson B. (2015) The origin of solutes  
1132 within the groundwaters of a high Andean aquifer. *Chemical Geology* **396**, 164-181.

1133 Roche M.A., Fernandez Jauregui C., Aliaga A., Bourges J., Cortes J., Guyot J.L., Pena J.  
1134 and Rocha N. (1991) Water and salt balances of the Bolivian amazon (Eds. Braga B.P.F.,  
1135 Fernandez Jauregui C.). UNESCO, Manaus, pp. 83–94.

1136 Rosner M., Erzinger J., Franz G. and Trumbull R.B. (2003) Slab- derived boron isotope  
1137 signatures in arc volcanic rocks from the Central Andes and evidence for boron isotope  
1138 fractionation during progressive slab dehydration. *Geochemistry, Geophysics,*  
1139 *Geosystems* **4**, 1–25.

1140 Rothstein D.A. and Manning C.E. (2003) Geothermal gradients in continental magmatic  
1141 arcs: Constraints from the eastern Peninsular Ranges batholith, Baja California, México.  
1142 In *Tectonic evolution of northwestern México and the southwestern USA: Boulder,*  
1143 *Colorado* (eds. Johnson S.E. et al.) *Geological Society of America Special Paper* **374**, pp.  
1144 337–354.

1145 Rouchon V., Courtial X., Durand I., Garcia B., Creon L. and Mougín P. (2016) A Fluid  
1146 Phase  
1147 Equilibria Model in the System CO<sub>2</sub>-N<sub>2</sub>-H<sub>2</sub>O-NaCl-He-Ne-Ar Below 200 Bar and 150°C  
1148 – Application to CO<sub>2</sub>/He Fractionation in Continental Mantle Degassing. Goldschmidt  
1149 Abstracts 2658.

1150 Ryu J. S., Vigier N., Lee S. W., Lee K. S. and Chadwick O. A. (2014) Variation of  
1151 lithium isotope geochemistry during basalt weathering and secondary mineral  
1152 transformations in Hawaii. *Geochimica et Cosmochimica Acta* **145**, 103-115.

1153 Salisbury M. J., Jicha B. R., de Silva S. L., Singer B. S., Jiménez N. C., and Ort M. H.  
1154 (2011) <sup>40</sup>Ar/<sup>39</sup>Ar chronostratigraphy of Altiplano-Puna volcanic complex ignimbrites  
1155 reveals the development of a major magmatic province. *Bulletin*, 123(5-6), 821-840.

1156 Sanford W.E. and Wood W.W. (1991) Brine evolution and mineral deposition in  
1157 hydrologically open evaporite basins. *American Journal of Science* **291**, 687-710.

1158 Sano Y. and Marty B. (1995) Origin of carbon in fumarolic gas from island arcs.  
1159 *Chemical Geology* **119**(1-4), 265-274.

1160 Sano Y., Takahata N., Nishio Y. and Marty B. (1998) Nitrogen recycling in subduction  
1161 zones. *Geophysical Research Letters* **25**, 2289-2292.

1162 Santoyo E., and Díaz-González L. (2010) A new improved proposal of the Na/K  
1163 geothermometer to estimate deep equilibrium temperatures and their uncertainties in  
1164 geothermal systems. Proceedings World Geothermal Congress, Bali, Indonesia.

1165 Servant-Vildary S. and Roux M. (1990) Multivariate analysis of diatoms and water  
1166 chemistry in Bolivian saline lakes. In: *Saline Lakes*. Springer, Dordrecht, pp. 267-290.

1167 Sanjuan B., Millot R., Ásmundsson R., Brach M. and Giroud N. (2014) Use of two new  
1168 Na/Li geothermometric relationships for geothermal fluids in volcanic environments.  
1169 *Chemical Geology* **389**, 60-81.

1170 Smith H.J., Spivack A.J., Staudigel H., and Hart S.R. (1995) The boron isotopic  
1171 composition of altered oceanic crust. *Chemical Geology* **126**, 119–135.

1172 Spiro B., Hoke L. and Chenery C. (1997) Carbon-isotope characteristics of CO<sub>2</sub> and CH<sub>4</sub>  
1173 in geothermal springs from the Central Andes. *International geology review* **39**(10), 938-  
1174 947.

1175 Springer M., and Förster, A. (1998). Heat-flow density across the central Andean  
1176 subduction zone. *Tectonophysics* **291**, 123-139.

1177 Stallard R. F. and Edmond J. M. (1981). Geochemistry of the Amazon: 1. Precipitation  
1178 chemistry and the marine contribution to the dissolved load at the time of peak discharge.  
1179 *Journal of Geophysical Research: Oceans* **86**(C10), 9844-9858.

1180 Strauss H. (1997) The isotopic composition of sedimentary sulfur through time.  
1181 *Palaeogeography, Palaeoclimatology, Palaeoecology* **132**(1-4), 97-118.

1182 Taylor B. E. (1986) Magmatic volatiles: isotopic variations of C, H and S stable isotopes  
1183 in high temperature geological processes. Reviews in Mineralogy 16 (eds. Valley J. W.,  
1184 Taylor H. P. and O’Neil J. R.) Mineral. Soc. America, pp. 185–225.

1185 Teboul P. A., Durllet C., Gaucher E. C., Virgone A., Girard J. P., Curie J., ... and Camoin  
1186 G. F. (2016) Origins of elements building travertine and tufa: New perspectives provided  
1187 by isotopic and geochemical tracers. *Sedimentary Geology* **334**, 97-114.

1188 Teboul P. A. (2017) Diagenesis of lower Cretaceous presalt continental carbonates from  
1189 the West African margin: simulations and analogues (Doctoral dissertation, Aix-  
1190 Marseille).

1191 Terra G.J.S., Spadini A.R., França A.B., Sombra C.L., Zambonato E.E., da Silva  
1192 Juschaks L.C., Arienti L.M., Erthal M.M., Blauth M., Franco M.P., Matsuda N.S., da  
1193 Silva N.G.C., Moretti Junior P.A., D’Avila R.S.F., de Souza R.S., Tonietto S.N., Couto  
1194 dos Anjos S.M., Campinho V.S. and Winter W.R. (2010) Classificação de rochas  
1195 carbonáticas aplicável às bacias sedimentares brasileiras. *Bulletin Geoscience Petrobras*,  
1196 *Rio de Janeiro* **18** (1), 9–29

1197 Thorpe R. S., Potts P. J., and Francis P. W. (1976) Rare earth data and petrogenesis of  
1198 andesite from the North Chilean Andes. *Contributions to Mineralogy and Petrology*  
1199 **54**(1), 65-78.

1200 Tosca N.J., Wright V.P. (2015) Diagenetic pathways linked to labile Mg-clays in  
1201 lacustrine carbonate reservoirs: a model for the origin of secondary porosity in the  
1202 Cretaceous Pre-salt Barra Velha Formation, Offshore Brazil, 435. Geological Society of  
1203 London, Special Publication. SP435-1.

1204 Verkouteren R. M. and Klinedinst D. B. (2004) Value Assignment and Uncertainty  
1205 Estimation of Selected Light Stable Isotope Reference Materials: RMs 8543-8545, RMs  
1206 8562-8564, and RM 8566. *NIST Special Publication* **260** (149), 59.  
1207 Verma S. P. and Santoyo E. (1995) New improved equations for Na/K and SiO<sub>2</sub>  
1208 geothermometers by error propagation. *Proc. World Geotherm. Congr* **2**, 963-968.  
1209 Verma, S. P. and Santoyo E. (1997) New improved equations for Na/K, Na/Li and SiO<sub>2</sub>  
1210 geothermometers by outlier detection and rejection. *Journal of Volcanology and*  
1211 *Geothermal Research* **79**(1-2), 9-23.  
1212 Verrecchia E.P. (2007) Lacustrine and palustrine geochemical sediments - Chapter 9. In:  
1213 Terrestrial geochemical sediments and geomorphology (Eds. D.J. Nash and S.J.  
1214 McLaren), Blackwell, London, Oxford, pp. 298-329.  
1215 Weinlich F. H., Bräuer K., Kämpf H., Strauch G., Tesař J. and Weise S. M. (1999) An  
1216 active subcontinental mantle volatile system in the western Eger rift, Central Europe: Gas  
1217 flux, isotopic (He, C, and N) and compositional fingerprints. *Geochimica et*  
1218 *Cosmochimica Acta* **63**(21), 3653-3671.  
1219 Zamanian K., Pustovoytov K. and Kuzyakov Y. (2016). Pedogenic carbonates: Forms  
1220 and formation processes. *Earth-Science Reviews* **157**, 1-17.  
1221 Zimmer M. M., Fischer T. P., Hilton D. R., Alvarado G. E., Sharp Z. D. and Walker J. A.  
1222 (2004). Nitrogen systematics and gas fluxes of subduction zones: insights from Costa  
1223 Rica arc volatiles. *Geochemistry, Geophysics, Geosystems* **5**(5).  
1224

## Figure Captions

1225

1226

1227 Fig. 1: **a.** Topographic map of Central Andes showing the location of Laguna Pastos  
1228 Grandes among the main Chilean and Bolivian salars (in white); **b.** Zoom into the  
1229 geological context of Laguna Pastos Grandes (modified from Bougeault et al., 2019);  
1230 satellite image provided by Zoom Earth website, © 2018 Microsoft Corporation Earthstar  
1231 Geographics SIO; **c.** View of the carbonate platform with partially immersed calcitic  
1232 pisoliths.

1233

1234 Fig. 2: Location of water and gas sampling in streams (blue stars), thermal springs (red  
1235 stars) and of the brine in one of the sustainable lakes (yellow star) in Laguna Pastos Grandes  
1236 (Bolivia). The location of volcanic rock samples is also shown with black dots. The four  
1237 thermal springs (images 1-4) flow up through the recent carbonate platform developing at  
1238 the west of the laguna. The arrows point to the bubbling gas in water basins, except for "El  
1239 Gigante" where gas and water have separate vents. Ign.: Ignimbrite; Dac.: Dacite; And.:  
1240 Andesite.

1241

1242 Fig. 3: Relative abundance of air-normalized isotope composition of noble gas ( $^4\text{He}$ ,  $^{20}\text{Ne}$ ,  
1243  $^{36}\text{Ar}$ ,  $^{40}\text{Ar}/^{36}\text{Ar}$  and  $^3\text{He}/^4\text{He}$ ) in thermal springs El Ojo Verde, La Rumba, La Salsa and El  
1244 Gigante. Normalization values used as references are 295.5 for  $^{40}\text{Ar}/^{36}\text{Ar}$  ratio (Nier, 1950)  
1245 and  $1.39 \times 10^{-6}$  for  $^3\text{He}/^4\text{He}$  ratio (Ozima and Podosek, 2002). Helium isotope ratios are  
1246 corrected for the effects of ASW (Air saturated Water) contamination in hydrothermal  
1247 system and are equivalent to  $R_c/R_a$ .

1248

1249 Fig. 4: Plot of  $\delta^{18}\text{O}$  versus  $\delta^2\text{H}$  for Pastos Grandes waters. Plot b is focused on thermal  
1250 springs (in red) and cold streams (in blue) in comparison with a rainfall sample (in white)  
1251 collected at the same altitude during the wet season in March 2017. Two samples of snow  
1252 (grey) were also collected during the dry season in January 2016. Data of rainfall and snow  
1253 are presented in Table A2. The composition of the lake brine (in yellow) of Pastos Grandes  
1254 is compared with the other Andean salars (in black, from this study and Boschetti et al.,  
1255 2007; Table A2). The Local Meteoric Water Line (LMWL; Chaffaut et al., 1998) and the  
1256 Local Ground- and Spring-Water Line (LGSWL; Rissmann et al., 2015) for the South-  
1257 Central Andes are also shown.

1258

1259 Fig. 5: Chemical compositions of Laguna Pastos Grandes water sources (thermal springs  
1260 in red/orange and streams in blue) and lake brine (in yellow). **a.** Schoeller diagram showing  
1261 relative concentrations in solutes; **b.** Plot of Ca versus Alkalinity (mM); **c.** Plot of Cl  
1262 concentration versus Cl/Br. Data from this study are reported with dots and previous data  
1263 with squares (Ballivian and Risacher, 1981; Hurlbert and Chang, 1984; Risacher and Fritz,  
1264 1991; Jones and Renaut, 1994).

1265

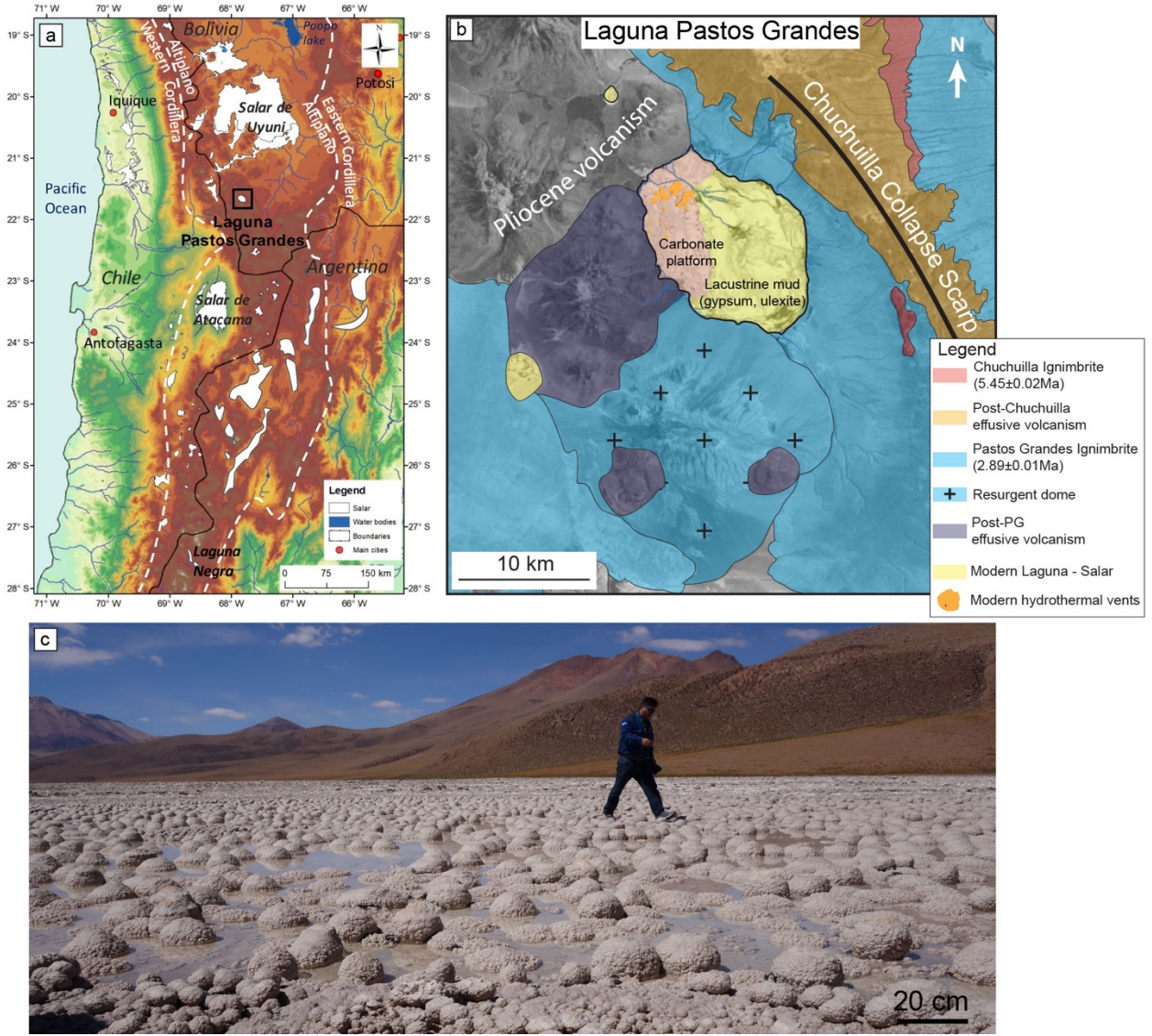
1266 Fig. 6: Sr, Li and B isotopic compositions of Laguna Pastos Grandes water sources (thermal  
1267 springs in red and streams in blue) and lake brine (in yellow) compared with andesite,  
1268 dacite (this study), and rhyolitic ignimbrite (this study and Kaiser, 2014) from the Pastos  
1269 Grandes caldera. **a.**  $^{87}\text{Sr}/^{86}\text{Sr}$  vs Sr concentration (mg/l) data compared with Cenomanian-  
1270 Turonian marine carbonates (McArthur et al., 1994) representing the last marine  
1271 sedimentary sequence in the central Andes region and modern marine evaporites (Pierret  
1272 et al., 2001). Mean values in Andean Central Volcanic Zone (CVZ) dacite (D) and andesite

1273 (A) are also shown for comparison (Cortecci et al., 2005); **b.**  $\delta^{11}\text{B}$  vs  $\delta^7\text{Li}$  data compared  
1274 with modern seawater (Boschetti et al., 2017) and rocks from the Andean volcanic arc  
1275 (Chan et al., 2002; Rosner et al., 2003).

1276  
1277 Fig. 7: Comparison of the water composition obtained for the volcanic bedrock weathering  
1278 at 200 (blue), 225 (red) and 250 °C (green) with increasing  $p\text{CO}_2$  from 10 bar in light color  
1279 to 100 bar in dark color. The average spring water is in black.

1280  
1281 Fig. 8: Conceptual model of modern carbonate precipitation in relation to the sources of  
1282 water and gas in Laguna Pastos Grandes. Violet-blue arrows refer to hydrothermal  
1283 circulations. See the conclusion for details. Data for boron isotopes are from De Hoog and  
1284 Savov (2018) for the Altered Oceanic Crust (AOC) and marine sediments and Marschall  
1285 (2018) for the mantle. Data for lithium isotopes are from Chan and Kastner (2000) for  
1286 subducted sediments, Moriguti and Nakamura (1998) and Chan et al. (1992) for AOC and  
1287 Misra et al. (2012) for the mantle. Data for nitrogen isotopes are from Ader et al. (2016)  
1288 for sediments and Sano et al. (1998) for the crust. Data for carbon isotopes are from Hoefs  
1289 (1980) for sedimentary organic carbon and Pineau and Javoy (1983) for mantle-derived  
1290 signature.  $R_c/R_a$  data are from Hoke et al (1994). Other data are from this study.

1291



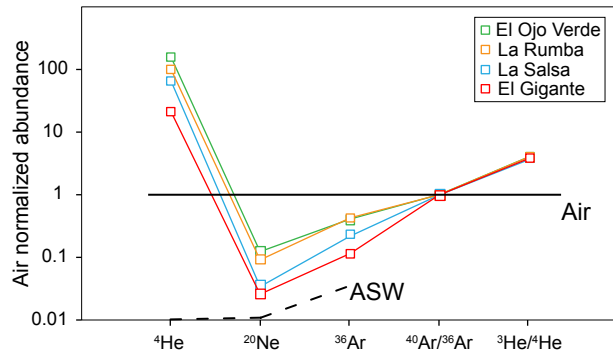
1292  
1293 Figure 1.





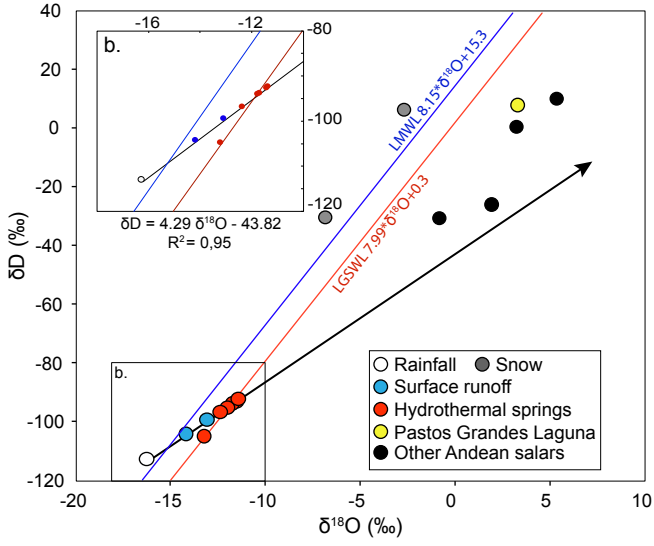
1294  
1295

Figure 2.



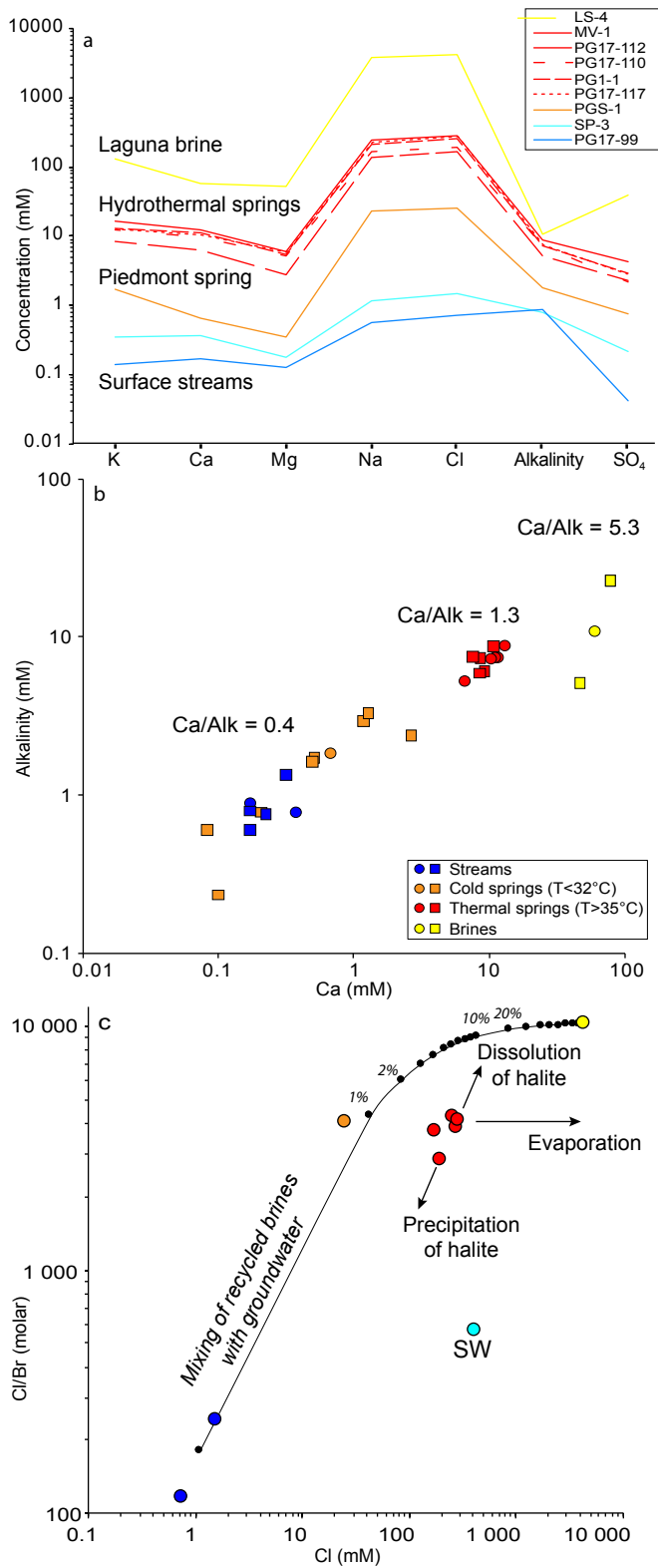
1296  
1297  
1298

Figure 3.



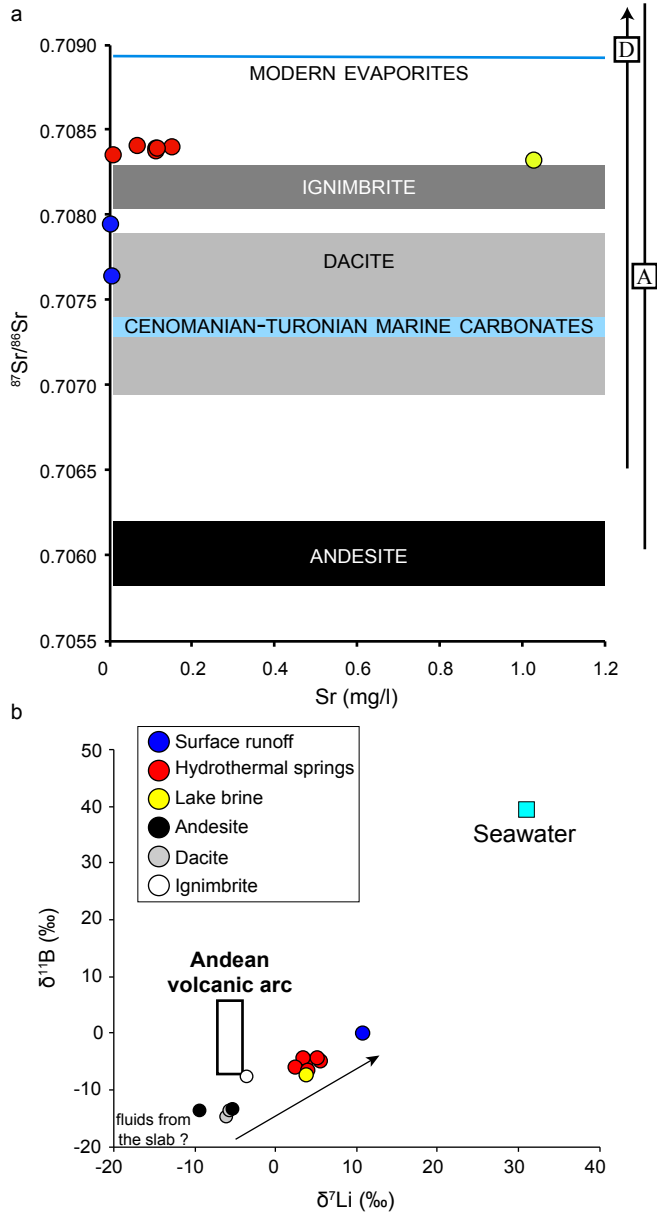
1299  
 1300  
 1301

Figure 4.



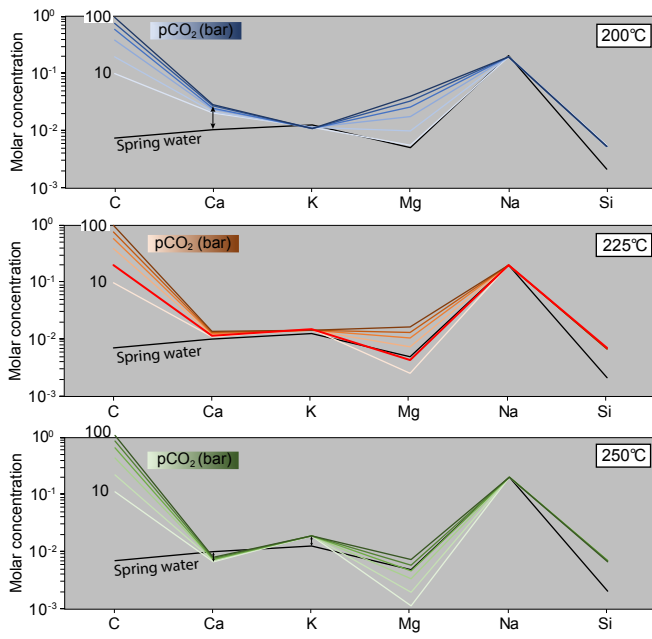
1302  
1303  
1304

Figure 5.



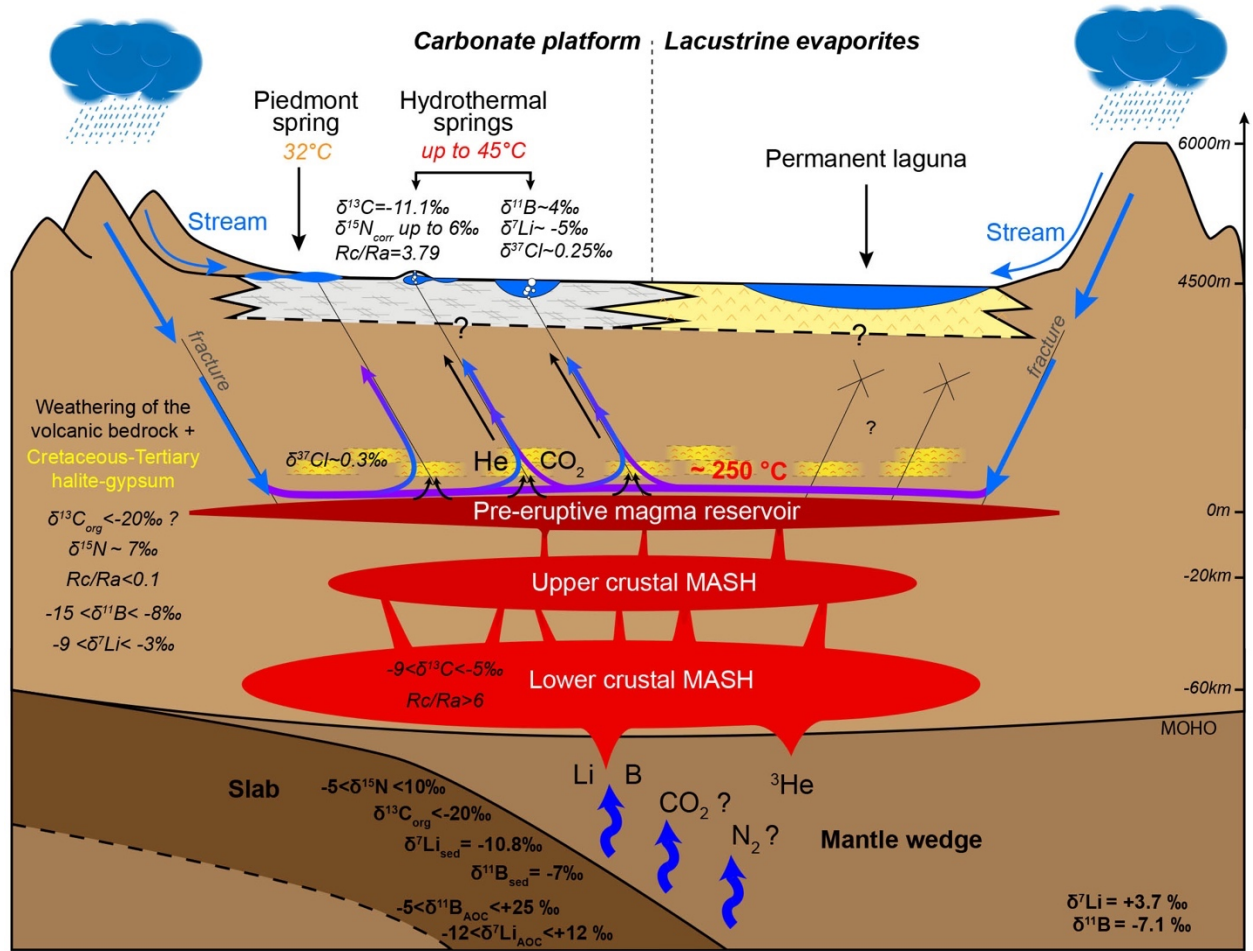
1305  
1306  
1307

Figure 6.



1308  
1309  
1310

Figure 7.



1311  
1312

Figure 8.

## Supplementary Material

1313  
1314  
1315  
1316  
1317  
1318  
1319  
1320  
1321  
1322  
1323  
1324  
1325  
1326  
1327  
1328  
1329  
1330  
1331  
1332  
1333  
1334  
1335  
1336  
1337  
1338  
1339

### PHREEQC modeling:

The mineralogical composition of the volcanic rocks sampled around the Laguna Pastos has been determined by DRX as:

- Dacite: alkali and potassium feldspar, quartz, biotite

- Andesite: alkali feldspar, biotite, olivine, amphibole

- Ignimbrite: alkali and potassium feldspar, quartz, biotite, amphibole

As numerous of these minerals are not available in the Thermoddem database, we performed the PHREEQC modeling with the selected minerals as follows:

*Solution 1*

*units mmol/l*

*temp 225 # Temperature varying between 200 and 250 °C*

*Equilibrium\_phases 1*

*Quartz(alpha) 0.0 10.0*

*Sanidine 0.0 10.0*

*Albite(low) 0.0 10.0*

*Anorthite 0.0 10.0*

*Pargasite 0.0 10.0*

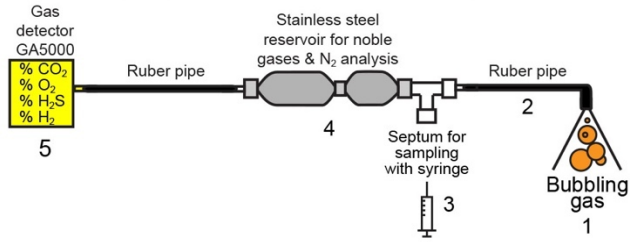
*Anhydrite 0.0 10.0*

*CO2(g) 1.3 #CO2(g) SI varying between 1-2*

*Halite 0.0 0.239 #Corresponding to the average Cl concentration in spring water*

*End*



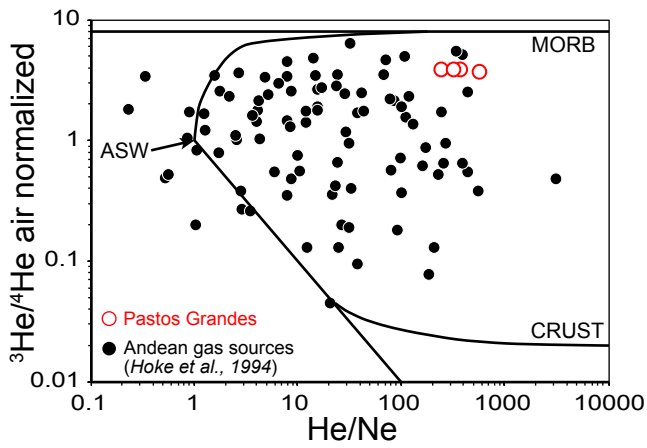


1340

1341 **Figure A1.** Photography and illustrating schema of bubbling gas sampling method.

1342

1343

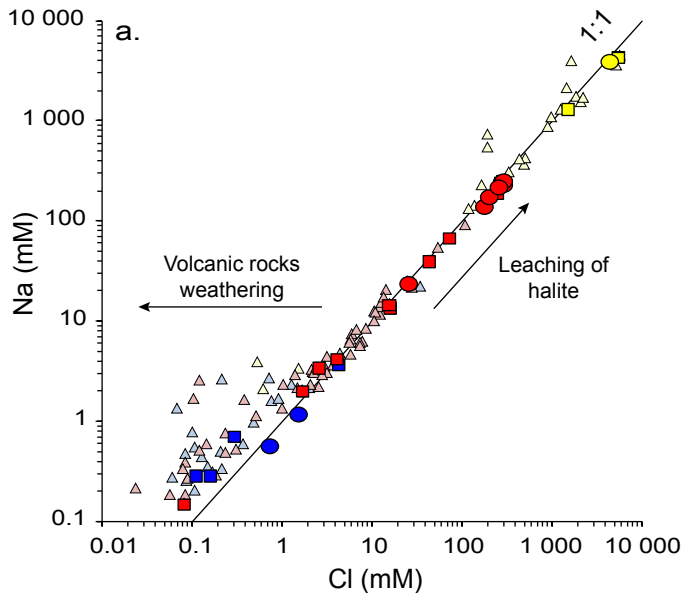


1344

1345 **Figure A2.** Air-normalized helium R/Ra values plotted against He/Ne ratios of gas samples  
 1346 from Laguna Pastos Grandes compared with other Andean sources (Hoke et al., 1994).

1347 Mixing lines between the three main sources of helium (crustal CRUST, mantle MORB  
 1348 and air saturated water ASW) are also represented.

1349



1350

1351 **Figure A3.** Relations between chloride and sodium for Pastos Grandes brines (in yellow)  
 1352 and water sources as a function of temperature: thermal spring >35 °C in red, <32 °C in  
 1353 orange and cold stream <15 °C in blue. Na-Cl compositions are compared with other  
 1354 Bolivian salars (pale triangles; Risacher and Fritz, 1991). Data from this study are reported  
 1355 with dots and previous data with squares (Ballivian and Risacher, 1981; Hurlbert and  
 1356 Chang, 1984; Risacher and Fritz, 1991; Jones and Renaut, 1994).

1357

1358 **Table A1.** Detailed nitrogen and carbon isotopic analysis of gas samples from Laguna  
 1359 Pastos Grandes.

Nitrogen analysis				
Sample	Date	Method	$\delta^{15}\text{N}$ (‰)	1 $\sigma$
PG100	20/07/2017	GC-IRMS on steel tube	2.73	0.03
PG100	20/07/2017	GC-IRMS on steel tube	2.75	0.01
PG112	20/07/2017	GC-IRMS on steel tube	1.79	0.02
PG112	20/07/2017	GC-IRMS on steel tube	1.77	0.01
PG112	07/02/2018	GC-IRMS on exetainer	1.74	0.02
PG116	07/02/2018	GC-IRMS on exetainer	1.60	0.02
PG117	19/07/2017	GC-IRMS on steel tube	2.49	0.05
PG117	19/07/2017	GC-IRMS on steel tube	2.47	0.03
PG117	19/07/2017	GC-IRMS on steel tube	2.24	0.03
PG117	19/07/2017	GC-IRMS on steel tube	2.26	0.02
PG117	19/07/2017	GC-IRMS on steel tube	2.18	0.02
PG117	19/07/2017	GC-IRMS on steel tube	2.17	0.02

Carbon analysis				
Sample	Date	Method	$\delta^{13}\text{C}$ (‰)	1 $\sigma$
PG100	14/06/2017	GC-C-IRMS	-11.36	0.01
PG100	14/06/2017	GC-C-IRMS	-11.32	0.01
PG100	14/06/2017	GC-C-IRMS	-11.31	0.01
PG100	20/07/2017	GC-IRMS	-10.73	0.03
PG100	20/07/2017	GC-IRMS	-11.27	0.03
PG112	14/06/2017	GC-C-IRMS	-11.31	0.01
PG112	14/06/2017	GC-C-IRMS	-11.24	0.01
PG112	14/06/2017	GC-C-IRMS	-11.26	0.01
PG112	20/07/2017	GC-IRMS	-11.11	0.03
PG112	20/07/2017	GC-IRMS	-11.24	0.03
PG116	14/06/2017	GC-C-IRMS	-11.25	0.03
PG116	14/06/2017	GC-C-IRMS	-11.08	0.03
PG116	14/06/2017	GC-C-IRMS	-11.05	0.03
PG116	07/02/2018	GC-IRMS	-11.00	0.04
PG116	07/02/2018	GC-IRMS	-11.49	0.04
PG116	07/02/2018	GC-IRMS	-11.43	0.06
PG117	14/06/2017	GC-C-IRMS	-11.06	0.04
PG117	19/07/2017	GC-IRMS	-10.85	0.05

1360 **Table A2.** Stable isotope compositions of Andean salars water, rainfall and snow from the  
1361 region of Pastos Grandes (from this study\* and Boschetti et al., 2007).

	$\delta^{18}\text{O}$ ( $\pm 0.1\text{‰}$ , 1s)	$\delta\text{D}$ ( $\pm 0.8\text{‰}$ , 1s)
Chaxa lagoon	-0.8	-30.5
Miñique lagoon	5.4	10.1
Miscanti lagoon	3.3	0.5
Uyuni*	1.9	-26.1
Rainfall*	-16.3	-112.9
Snow 1*	-6.8	-30.3
Snow 2*	-2.7	6.5

1362

1363

1364

1365

1366 **Table A3.**  $\delta^{37}\text{Cl}$  analyses of water samples from Laguna Pastos Grandes.

Sample	$\delta^{37}\text{Cl}$ (‰)	1 $\sigma$
La Salsa 1	0.308	0.002
La Salsa 2	0.230	0.010
La Salsa 3	0.230	0.009
La Salsa 4	0.260	0.009
La Salsa 5	0.234	0.003
La Salsa 6	0.292	0.002
La Salsa 7	0.300	0.002
La Rumba 1	0.227	0.010
La Rumba 2	0.205	0.006
La Rumba 3	0.234	0.011
El Ojo Verde 1	0.246	0.009
El Ojo Verde 2	0.252	0.013
<b>Average</b>	<b>0.251</b>	<b>0.032</b>

1367

1368 **Table A4.** Results of PHREEQC modeling. Alb. Albite(low); Anh. Anhydrite; An. Anorthite; Hal. Halite; Par. Pargasite; Qtz.  
 1369 Quartz(alpha); San. Sanidine

	pCO <sub>2</sub> (bar)	Alb.	Anh.	An.	CO2(g)	Hal.	Par.	Qtz	San.		C	Ca	Cl	K	Mg	Na	S	Si
Input temperature: 200 °C	10	4.9E-2	-5.0E-4	-1.7E-2	-1.0E-1	-2.4E-1	-1.4E-3	-7.6E-2	-1.1E-2	Water chemistry (molality)	1.0E-1	2.0E-2	2.4E-1	1.1E-2	5.6E-3	1.9E-1	5.0E-4	5.4E-3
	20	5.0E-2	-5.3E-4	-1.6E-2	-2.0E-1	-2.4E-1	-2.4E-3	-7.6E-2	-1.1E-2		2.0E-1	2.1E-2	2.4E-1	1.1E-2	9.8E-3	1.9E-1	5.3E-4	5.4E-3
	40	5.2E-2	-5.7E-4	-1.4E-2	-3.9E-1	-2.4E-1	-4.4E-3	-7.4E-2	-1.1E-2		3.9E-1	2.3E-2	2.4E-1	1.1E-2	1.8E-2	1.9E-1	5.7E-4	5.4E-3
	60	5.4E-2	-6.0E-4	-1.2E-2	-5.8E-1	-2.4E-1	-6.3E-3	-7.2E-2	-1.1E-2		5.8E-1	2.5E-2	2.4E-1	1.1E-2	2.5E-2	1.9E-1	6.0E-4	5.3E-3
	80	5.5E-2	-6.3E-4	-9.9E-3	-7.6E-1	-2.4E-1	-8.1E-3	-6.9E-2	-1.1E-2		7.6E-1	2.7E-2	2.4E-1	1.1E-2	3.2E-2	1.9E-1	6.3E-4	5.3E-3
	100	5.7E-2	-6.6E-4	-7.8E-3	-9.6E-1	-2.4E-1	-1.0E-2	-6.7E-2	-1.1E-2		9.6E-1	2.9E-2	2.4E-1	1.1E-2	4.0E-2	1.9E-1	6.6E-4	5.3E-3
Input temperature: 225 °C	10	3.6E-2	-4.5E-4	-9.4E-3	-1.0E-1	-2.4E-1	-6.4E-4	-4.7E-2	-1.5E-2		1.0E-1	1.1E-2	2.4E-1	1.5E-2	2.6E-3	2.0E-1	4.5E-4	7.2E-3
	20	3.6E-2	-4.7E-4	-8.9E-3	-2.0E-1	-2.4E-1	-1.1E-3	-4.6E-2	-1.5E-2		2.0E-1	1.2E-2	2.4E-1	1.5E-2	4.4E-3	2.0E-1	4.7E-4	7.1E-3
	40	3.7E-2	-4.9E-4	-8.1E-3	-4.0E-1	-2.4E-1	-1.9E-3	-4.5E-2	-1.5E-2		4.0E-1	1.2E-2	2.4E-1	1.5E-2	7.7E-3	2.0E-1	4.9E-4	7.1E-3
	60	3.7E-2	-5.1E-4	-7.2E-3	-6.0E-1	-2.4E-1	-2.7E-3	-4.4E-2	-1.5E-2		6.0E-1	1.3E-2	2.4E-1	1.5E-2	1.1E-2	2.0E-1	5.1E-4	7.0E-3
	80	3.8E-2	-5.2E-4	-6.3E-3	-7.9E-1	-2.4E-1	-3.4E-3	-4.3E-2	-1.5E-2		7.9E-1	1.4E-2	2.4E-1	1.5E-2	1.4E-2	2.0E-1	5.2E-4	7.0E-3
	100	3.8E-2	-5.4E-4	-5.4E-3	-9.9E-1	-2.4E-1	-4.2E-3	-4.1E-2	-1.5E-2		1.0E0	1.4E-2	2.4E-1	1.5E-2	1.7E-2	2.0E-1	5.4E-4	6.9E-3
Input temperature: 250 °C	10	3.2E-2	-4.3E-4	-5.8E-3	-1.1E-1	-2.4E-1	-3.0E-4	-3.1E-2	-1.9E-2		1.1E-1	6.8E-3	2.4E-1	1.9E-2	1.2E-3	2.1E-1	4.3E-4	7.3E-3
	20	3.2E-2	-4.4E-4	-5.6E-3	-2.2E-1	-2.4E-1	-5.0E-4	-3.1E-2	-1.9E-2		2.2E-1	7.0E-3	2.4E-1	1.9E-2	2.0E-3	2.1E-1	4.4E-4	7.2E-3
	40	3.2E-2	-4.5E-4	-5.2E-3	-4.5E-1	-2.4E-1	-8.6E-4	-3.0E-2	-1.9E-2		4.5E-1	7.3E-3	2.4E-1	1.9E-2	3.5E-3	2.1E-1	4.5E-4	7.2E-3
	60	3.3E-2	-4.6E-4	-4.8E-3	-6.7E-1	-2.4E-1	-1.2E-3	-3.0E-2	-1.9E-2		6.7E-1	7.6E-3	2.4E-1	1.9E-2	4.8E-3	2.1E-1	4.6E-4	7.1E-3
	80	3.3E-2	-4.7E-4	-4.4E-3	-8.8E-1	-2.4E-1	-1.5E-3	-2.9E-2	-1.9E-2		8.9E-1	7.9E-3	2.4E-1	1.9E-2	6.1E-3	2.1E-1	4.7E-4	7.1E-3
	100	3.3E-2	-4.7E-4	-4.0E-3	-1.1E0	-2.4E-1	-1.8E-3	-2.9E-2	-1.9E-2		1.1E0	8.2E-3	2.4E-1	1.9E-2	7.3E-3	2.1E-1	4.7E-4	7.0E-3

1370

1371

1372